

Stony Brook University



OFFICIAL COPY

The official electronic file of this thesis or dissertation is maintained by the University Libraries on behalf of The Graduate School at Stony Brook University.

© All Rights Reserved by Author.

A First-Principles Study of Thiol Ligated CdSe Nanoclusters

A Dissertation Presented

by

Shanshan Wu

to

The Graduate School in Partial Fulfillment of the Requirements for the Degree of

Doctor of Philosophy

in

Applied Mathematics and Statistics

Stony Brook University

August 2012

Stony Brook University

The Graduate School

Shanshan Wu

We, the dissertation committee for the above candidate for the
Doctor of Philosophy degree, hereby recommend
acceptance of this dissertation.

James Glimm – Dissertation Advisor
Professor of Applied Mathematics and Statistics

Roman Samulyak - Chairperson of Defense
Associate Professor of Applied Mathematics and Statistics

Xiangming Jiao - Committee of Defense
Associate Professor of Applied Mathematics and Statistics

Michael McGuigan - Committee of Defense
Active Director of Computational Science Center, Brookhaven National Lab

This dissertation is accepted by the Graduate School

Charles Taber
Interim Dean of the Graduate School

Abstract of the Dissertation

A First-Principles Study of Thiol Ligated CdSe Nanoclusters

by

Shanshan Wu

Doctor of Philosophy

in

Applied Mathematics and Statistics

Stony Brook University

2012

A first-principles study of small Cd_nSe_n Quantum Dots (QD) ($n = 6, 12, 13, \text{ and } 33$) has been performed for application to QD solar cell development. A validation of the DFT methodology is carried out to justify the choices of basis sets and DFT exchange and correlation functional. We separately assess the effects of the particle size and the passivating ligands upon the optimized structure and the energy gap (from a density functional theory (DFT) calculation) and the corresponding absorption spectrum (from a time-dependent density functional theory (TDDFT) calculation). The structures of four thiol ligands, namely — cysteine (Cys), mercaptopropionic acid (MPA), and their reduced-chain analogues, are investigated. We have documented significant passivation

effects of the surfactants upon the structure and the optical absorption properties of the CdSe quantum dots: The surface Cd-Se bonds are weakened, whereas the core bonds are strengthened. A blue shift of the absorption spectrum by ~ 0.2 eV is observed. Also, the optical absorption intensity is enhanced by the passivation. By contrast, we have observed that varying the length of ligands yields only a minor effect upon the absorption properties: a shorter alkane chain might induce a slightly stronger interaction between the $-\text{NH}_2$ group and the nearest surface Se atom, which is observed as a stronger ligand binding energy. For $\text{Cd}_{12}\text{Se}_{12}$, which is regarded as the ‘non-magic’ size QD, neither the self-relaxation nor the ligand passivation could fully stabilize the structure or improve the poor electronic properties. We also observe that the category of thiol ligands possesses a better ability to open the band gap of CdSe QD than either phosphine oxide or amine ligands. Our estimation of the absorption peak of the Cys-capped QDs ranges from 413 nm to 460 nm, which is consistent to the experimental peak as 422 nm.

Table of Contents

Table of Contents	v
List of Figures.....	viii
List of Tables	x
Acknowledgments	xiii
Chapter 1 Introduction.....	1
1.1 Survey of Renewable Energy.....	1
1.2 Quantum Dot Sensitized Solar Cells (QDSSC)	4
1.3 Research Background and Motivation	6
1.4 Main Results and Outline for Chapters	7
Chapter 2 Physical Theories	9
2.1 Time-independent Schrödinger equation	9
2.2 Hartree-Fock Method	11
2.3 Møller-Plesset Perturbation Theory Second-order Correction	13
2.4 Coupled Cluster Approximation	14
2.5 Density Functional Theory.....	15
2.6 Linear Combinations of Atomic Orbitals.....	20

2.7 Local Basis Functions	21
2.8 Time Dependent Density Functional Theory (TDDFT)	22
2.9 Mulliken Population Analysis	24
2.10 Gaussian Broadening Approach.....	25
2.11 Density of States (DOS) and Projected DOS	25
2.12 Fermi's Golden Rule	26
Chapter 3 Computational Model.....	28
3.1 Design of Simulation Model	28
3.2 Simulation Methodology.....	29
3.3 Geometry Optimization of QDs.....	30
3.4 Verification and Validation of Simulation.....	31
Chapter 4 Simulation Results	33
4.1 Bare Quantum Dots.....	33
4.2 Quantum Dots Capped by Organic Ligands	35
4.3 Optical Properties of QDs	43
Chapter 5 Conclusions.....	52
Bibliography	54

Appendix.....	59
A1. Geometry Optimization of Bare and Passivated QDs.....	59
A2. Optical Properties of Bare and Passivated QDs.....	59

List of Figures

Figure 1.1: Growth Rates of Renewable Energy.	2
Figure 1.2: Renewable Energy Share of Global Final Energy Consumption, 2009 Energy Capacity.....	3
Figure 1.3: Cost of Electricity by Source.....	3
Figure 1.4: Efficiency of different Photovoltaic solar cells.....	5
Figure 3.1: Structures of Four Sizes CdSe Quantum Dots and Crystal Bulk (Cd: cyan, Se: yellow).....	28
Figure 3.2: Structures of MPA and Cys and Their Reduced Chain Analogy (S: orange, N: blue, C: gray, O: red, H: white).....	29
Figure 3.3: Absorption Peak of Cys-capped Cd ₃₃ Se ₃₃ . Left: Experimental result ¹⁰ ; Right: Simulation Estimation.....	32
Figure 4.1. (a) Band gap value and binding energy per Cd-Se pair and (b) Density of states (DOS) of different size bare Cd _n Se _n QDs ('n' = 6, 12, 13, and 33) calculated using the B3LYP / LANL2dz methodology. The Fermi energy has been chosen to be in the middle of the HOMO-LUMO gap and a Gaussian broadening of 0.1 eV has been used for the DOS calculations in (b).	34

Figure 4.2. Density of states (DOS) of Cd_6Se_6 with four ligands calculated using the B3LYP / (LANL2dz/6-31G*) method. The Fermi energy is set in the middle of the HOMO-LUMO gap, and a Gaussian broadening of 0.05 eV has been used for the DOS calculations.46

Figure 4.3. Absorption spectra for (a) Cd_6Se_6 with four different ligands, (b) $\text{Cd}_{13}\text{Se}_{13}$ with four different ligands, (c) bare $\text{Cd}_{33}\text{Se}_{33}$. The B3LYP / (LANL2dz/6-31G*) method is used for the TDDFT calculation. A Gaussian broadening of 0.05 eV has been used.47

List of Tables

Table 3.1: Comparing Results of Bond Length and Energy Gap with Reference Data (in the parentheses). All the calculation is using LANL2DZ basis set and B3LYP exchange and correlation functional.....	32
Table 4.1. Optimized structures of Cd_nSe_n + Ligands ('n' = 6, 12, 13, and 33) using the B3LYP functional theory with the LANL2DZ/6-31G* (CdSe/Ligand) basis sets (Cd: cyan, Se: yellow, H: white, S: orange, C: gray, O: red, N: blue)...	38
Table 4.2. Species of Cd_nSe_n ('n' = 6, 12, 13, 33) + Ligands calculated using B3LYP functional with LANL2DZ/6-31G* (CdSe/Ligand) basis sets.....	41
Table 4.3. Decomposition of the representative TDDFT excited-states of Cd_nSe_n ('n' = 6, 13) with four ligands and bare $Cd_{33}Se_{33}$. A full list of transition states of capped Cd_6Se_6 is in Table A. 3.	48
Table 4.4. The isosurface of wavefunction superimposed on the atomic structure of bare and capped QDs. The selected states are all active in the excitation as shown in Table 4.3.....	50
Table A. 1: Band gap value and binding energy per Cd-Se pair for different sized bare CdSe quantum dots. All the quantum dots have been relaxed using PBE and B3LYP functional, respectively. The B3LYP functional results in a slightly smaller HOMO-LUMO gap and binding energy per CdSe pair than does the PBE	

functional. The band gap values for Cd₆Se₆ and Cd₁₃Se₁₃ obtained by using the B3LYP functional are 3.14 eV and 3.06 eV, respectively, which are in good agreement with earlier results ^{17, 18, 44}.60

Table A. 2. Cd_nSe_n ('n' = 6, 12, 13, 33) + Ligands calculated by using the PBE and B3LYP functional theories with the LANL2DZ/6-31G* (CdSe/Ligand) basis sets. Two XC functionals, PBE and B3LYP, show the same trend in all of the QDs tested. The B3LYP functional results slightly in a smaller HOMO-LUMO gap and binding energy of ligand than the PBE functional does. The average bond length of Cd₆Se₆ has been computed to be 2.699 Å / 2.862 Å for intra/inter layer Cd-Se by using the B3LYP functional, which are consistent with the results of P. Yang ¹⁷ and A. Kuznetsov ¹⁸. Use of the B3LYP functional results in a quantitatively better description for the bond length and a closer fit to reference results than analogous use of the PBE functional. Thus, all of our later discussion is based on the geometry relaxed by using the B3LYP functional.61

Table A. 3: Decomposition of the representative TDDFT excited-states of Cd₆Se₆ with four ligands. Most of the orbitals possessing dominant contributions to the excitations are localized on the Cd₆Se₆ QDs rather than on the ligands. This observation agrees well with Kilina's work ¹⁴. This observation could therefore explain the relatively minor influence of different ligands upon the observed absorption spectrum. For bare and capped Cd₆Se₆, all of the transitions occurred

among the same orbitals (Here the degenerate states are considered as the same states). Hence, the surface passivation shifts the optical spectra of the bare Cd₆Se₆ QDs to the blue by ~0.2 eV.64

Acknowledgments

I am deeply indebted to my supervisor Prof. James Glimm whose instruction, stimulating suggestions and encouragement helped me in all the time for the researching and writing of this dissertation. Specially, I would like to thank to Dr. Michael McGuigan (BNL), Dr. Yan Li (BNL) and Dr. Xiaolin Li for their mentoring of my research during my PhD time. I would like to express appreciation to my committee Prof. Roman Samulyak, Dr. Michael Mcguigan and Prof. Xiangmin Jiao, who very pleasantly accepted my request to serve on my dissertation committee and offered valuable suggestions to improve the dissertation.

I would like to acknowledge financial support for this work provided by Stony Brook University and Brookhaven National Lab Seed Grant. The text of this dissertation in part is a reprint of the materials as it appears in arXiv:1207.5408v1, which has been submitted for reviewing. The co-authors listed in the publication directed and supervised overall research project that forms the basis for this dissertation.

I would like to thank the National Energy Research Scientific Computing (NERSC) Center to offer the computational resources to this work. The machine is supported by the Office of Science of the U.S. Department of Energy under Contract No. DE-AC02-05CH11231. This dissertation also utilized resources at

the New York Center for Computational Sciences at Stony Brook University / Brookhaven National Laboratory which is supported by the U.S. Department of Energy under Contract No. DE-AC02-98CH10886 and by the State of New York.

I would like to express my gratitude to my parents and my fiancé, who never hesitate to give me their care, support and love. I would also appreciate all the support from my friends, classmates, and workmates in both Stony Brook University and Brookhaven National Lab. I will always remember the great times we shared together.

Chapter 1

Introduction

1.1 Survey of Renewable Energy

As we know, the carbon-based energy sources will be used up in the near future ¹. Finding the replacement has been the world's biggest energy problem. The renewable energy, coming from natural sources such as sunlight, wind, water and tides, definitely has great potential. Renewable energy is clean and has no carbon-emission. The energy sources are naturally replenished. Figure 1.1 ² and Figure 1.2 ² show that the global renewable energy capacity growing strongly and steadily in last 5 years and renewable energy provides 16% of the total energy consumption in 2010. With fossil fuel running out and the development of renewable energy technology, this percentage of renewable energy will most likely keep going up in the future.

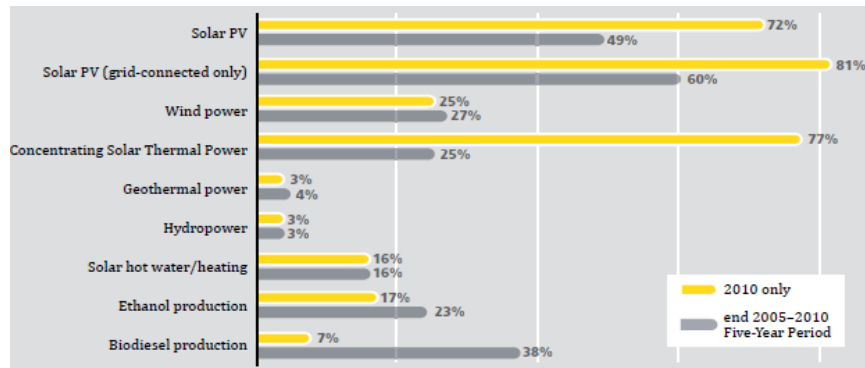


Figure 1.1: Growth Rates of Renewable Energy.

Compared to wind, biomass, geothermal and traditional fuel energy, solar energy do has certain advantages ¹. The total power of sunlight reaching the earth is about 101, 000 terawatts, while the whole world consumes 15 terawatts now each year. The power of sunlight is more than sufficient to supply the total energy needs now and in the future. Although sunlight cannot deliver energy in a dense way as traditional fuels, solar energy has its advantage over biomass and wind: Solar energy is also environment friendly. It has little carbon-emission and water-consumption. Due to all these potentials, solar energy has drawn huge attention from governments and companies ². According to Figure 1.1, Solar Photovoltaic keeps a high growth rate in the last five years. Now, the main limit of solar energy is the cost. Figure 1.3 ³ shows that the electricity cost of photovoltaic solar cell is much higher than other renewable energy resources. However, with the development of technology and materials science, especially the improvement of

nanotechnology, the cost of photovoltaic solar cell is expected to drop dramatically in the next decades compared to other energy resources.

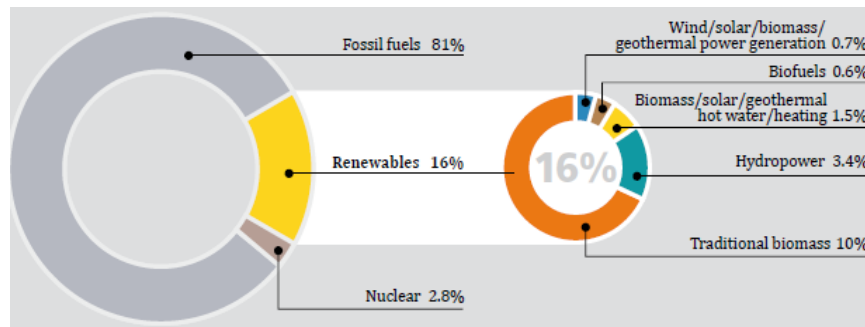


Figure 1.2: Renewable Energy Share of Global Final Energy Consumption, 2009 Energy Capacity.

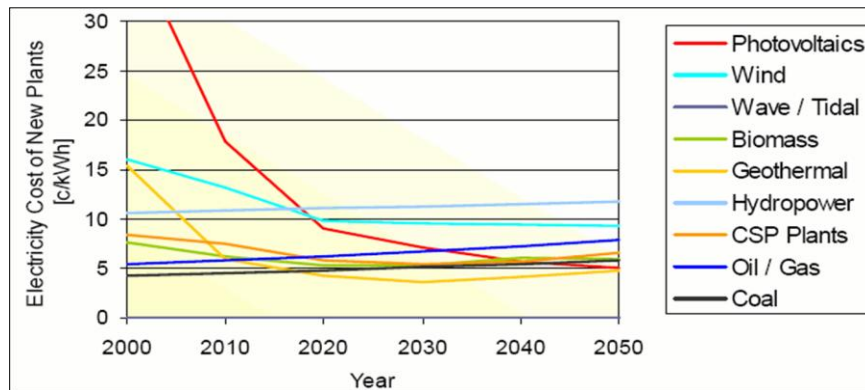


Figure 1.3: Cost of Electricity by Source.

1.2 Quantum Dot Sensitized Solar Cells (QDSSC)

Photovoltaic solar cells are commonly classified as first-, second- and third-generation devices. Most of the devices on the market now are first and second generation cells, which are based on crystalline silicon and CdTe thin film, respectively. High purity requirements for the silicon crystals, high fabrication temperatures and the large amount of material which is needed are major cost factors, while the thermodynamic limit of the light to electric power conversion efficiency is another limitation to the first and second generation solar cells. Figure 1.4 shows the efficiency of different generation Photovoltaic solar cells.

As one of the third-generation solar cells, quantum dot (QD) sensitized solar cell has drawn great attentions these days. In the design of QDSSC, the active element is the quantum dot composed of semi-conducting material, such as CdSe, Si, Ge and GaAs. These semi-conducting elements have a band gap which determines the energy level of electrons excited by incoming photons. CdSe–TiO₂ composite quantum dots (QDs) are an example of a QD sensitized solar cell constituent. Comparing with the traditional first- and second-generation solar cell, QDSSC possesses several advantages: firstly, the QDs can be produced by low-cost method; secondly, its absorption spectrum can be tailored by controlling the size. By using these optical properties of QDs, we could build impurity band cells to full cover the whole solar spectrum ^{4, 5}, which might enable the excess of the

thermodynamic limit. Due to their distinctive optical properties, QD-sensitized solar cells have been investigated intensively^{4, 6-10}. However, only 12% efficiency has been reached in experiments^{6, 10}. The research of quantum dot solar cells is still ongoing and the expensive cost of experiments also limits the further development of research. The factors limiting the efficiency of solar devices and the detailed physical mechanism of the photovoltaic process, however, are only partially understood. The main research interests are focused on these aspects: the first one is the size and shape control of QDs by different surfactants and manufacture environment; the second one is the effects of surfactants and coating by other materials on the electronic and optical properties of QDs; another important issue is to improve the attachment of QDs to the TiO₂ substrate and increase the electron transmission efficiency. In this project, we mainly focus on the effects of surfactants on the electronic and optical properties of QDs.

Materials	Efficiency
Crystalline	12 – 40%
Thin film	7 – 10%
Quantum Dot	12%

Figure 1.4: Efficiency of different Photovoltaic solar cells

1.3 Research Background and Motivation

Surface passivation of CdSe QDs has always been a central issue for the optical properties of QDSSC. Many experimental^{6, 8, 10-12} and theoretical¹³⁻¹⁷ studies have been performed. Nevins *et al.*¹⁰ reports that cysteine (Cys) passivation could produce a ‘magic size’ CdSe QD of around 2nm in diameter in solvent when the pH is > 13, whereas the use of mercaptopropionic acid (MPA) produces a larger and ‘non-magic’ size QD. The Cys-capped ‘magic size’ QDs exhibit a narrow and intense first excitonic absorption peak, as compared with the ‘non-magic’ size QDs capped with MPA. These authors report that the amine group plays a crucial role in controlling the QD size. However, besides stabilizing the QDs¹⁰, the effect of the amine group on the absorption properties of QDs has not been properly investigated.

Many theoretical studies have been performed on bare and capped CdSe QDs. Reference¹⁸ provides a full summary of previous work on the CdSe QDs saturated by different kinds of ligands. However, no systematic work has been performed on comparing the optical consequence of using Cys and MPA ligands on CdSe QDs. Reference¹⁹ has studied the effects of Cys and MPA bonded on a single Cd-Se pair in aqueous phase on its absorption spectrum, but no studies of either completely or partially capped CdSe QDs have been performed. Reference²⁰ focuses on Cys and Cys-Cys dimer binding as well as hydrogen passivation

effects on the CdSe QD geometries and the corresponding excitation spectra. The carboxyl group is the active part of ligand that is bonded to the Cd atom. Reference ¹⁸ reports on the MPA passivation effects on only an isolated Cd₆Se₆ cluster.

1.4 Main Results and Outline for Chapters

In this thesis, we present a first-principles study of the full surface ligation of CdSe QDs with Cys and MPA. We test these two typical ligands on different sizes of Cd_nSe_n QDs with ‘n’ = 6, 12, 13, and 33. The ligand length effect on the optical properties of the QDs has also been investigated. The study is based on the density functional theory (DFT) and time-dependent density functional theory (TDDFT) analyses. A geometry optimization, based on DFT theory, has been applied to the raw QDs in order to minimize surface dangling bonds. We have determined the ground state band gap as well, in addition to the binding energy and bond length of the relaxed structures. When capping the Cd₃₃Se₃₃ by the thiol category ligands, an increase of HOMO-LUMO gap by 0.28 eV is obtained, whereas increases of ~0.14 eV and of ~0.19 eV are reported for OPMe₃ and NH₂Me capped QDs, respectively ¹⁴. A TDDFT calculation has been carried out in order to compute the optical absorption spectrum. We have observed a constant blue shift of ~0.2 eV when adding the ligands to the bare QDs. Varying the

lengths of ligands yields only a minor impact upon the observed absorption, which is consistent with the experimental results, has been noted for both MPA and MDA⁶. The amine group might have stabilizing effects on the QD. However, little influence has been observed on the absorption spectrum. Our estimation of the absorption peak of Cys-capped Cd₃₃Se₃₃ is arranged from 413 nm to 460 nm, which is quite close to the experimentally observed absorption peak of magic-size Cys-capped CdSe QDs as 422 nm¹⁰. A theoretical explanation for all of these results in terms of local density of states and isosurface plots of wavefunction is offered.

In Chapter 2, we introduce the physical model and in Chapter 3, we verify the simulation methodology. In Chapter 4, we analyze the simulation results and compare these with previous work. In Chapter 5, we draw conclusions for the effects of surface surfactants and QD sizes upon the electronic and optical properties of the QDs.

Chapter 2

Physical Theories

2.1 Time-independent Schrödinger equation

The stationary states of the many body system are described by the time-independent Schrödinger equation,

$$H\Psi = E\Psi \quad (2.1.1)$$

When the Hamiltonian operator acts on the wavefunction Ψ , and if the result is proportional to Ψ , we call Ψ is a stationary state. The proportionality constant E is called the energy state of wavefunction Ψ .

The Hamiltonian is composed of five terms,

$$H = T_n + T_e + V_{int} + V_{ext} + V_{nn} \quad (2.1.2)$$

Here, we use atomic units throughout this thesis, so that

$$e^2 = \hbar = m = 1 \quad (2.1.3)$$

where e is the electronic charge, \hbar is Planck's constant, and m is the electronic mass. T_n and T_e are the kinetic energy operator for the nuclear and electrons defined as

$$T_n = -\frac{1}{2} \sum_A^M \nabla_A^2 \quad (2.1.4)$$

$$T_e = -\frac{1}{2} \sum_i^N \nabla_i^2 \quad (2.1.5)$$

M is the number of nuclei and N is the number of total electrons. V_{int} is the electron-electron Coulomb interaction potential,

$$V_{int} = \frac{1}{2} \sum_i^N \sum_{i \neq j}^N \frac{1}{|r_i - r_j|} \quad (2.1.6)$$

Here, r_i is the coordinate of electron i and the charge on the nucleus A at r_A is Z_A .

V_{ext} is the external potential due to positively charged nuclei,

$$V_{ext} = - \sum_i^N \sum_A^M \frac{Z_A}{|r_i - r_A|} \quad (2.1.7)$$

V_{nn} is the nuclear interaction potential,

$$V_{nn} = \frac{1}{2} \sum_A^M \sum_{A \neq B}^M \frac{1}{|r_A - r_B|} \quad (2.1.8)$$

Due to the masses of the nuclei are much heavier than them of the electrons, and the nuclei moves much slower than the electrons, so we can consider the electrons as moving in the field of fixed nuclei. In this case, the nuclear kinetic energy is zero and their potential energy is merely a constant. The potential energy has no effect on the wavefunctions and only shifts the values of eigenstate. Thus, we can ignore T_n and V_{nn} , and the Hamiltonian operator is simplified to a sum of three terms,

$$H = T_e + V_{int} + V_{ext}. \quad (2.1.9)$$

This is the Born-Oppenheimer approximation.

2.2 Hartree-Fock Method

The ground state wavefunction Ψ_0 could be searched by the variational principle,

$$E_0[\Psi_0] = \min_{\Psi} E[\Psi] = \min_{\Psi} \langle \Psi | H | \Psi \rangle, \quad \langle \Psi | \Psi \rangle = 1 \quad (2.2.1)$$

The variational principle states that we can use any normalized wavefunction Ψ to calculate the total energy E for the system, and the result energy is an upper bound to the true ground-state energy E_0 .

However, the wave function depending on $3N$ coordinates is very difficult to solve even for N larger than 2, due to the coupled interaction term V_{int} . To simplify the computation, we assume every single electron is non-interacting with others. In this case, the wavefunction Ψ is denoted by a single Slater determinant of occupied orbitals φ_i ,

$$\Psi = \frac{1}{\sqrt{N!}} \begin{vmatrix} \varphi_1(x_1) & \cdots & \varphi_1(x_N) \\ \vdots & & \vdots \\ \varphi_N(x_1) & \cdots & \varphi_N(x_N) \end{vmatrix} \quad (2.2.2)$$

It's easy to prove that the wavefunction satisfies the Pauli Exclusion Principle. Here $x_i = \{r_i, \sigma_i\}$, where σ_i is the spin coordinate of the i th electron. For a single spin molecule, the same orbital function is used for both α and β spin electrons in each pair, which is called restricted Hartree-Fock (HF) method. For open shell molecules, we have unrestricted HF and restricted open HF. The HF energy could be simplified as

$$E_{HF} = \sum_i^N \langle \varphi_i | h_1 | \varphi_i \rangle + \frac{1}{2} \sum_{i,j}^N [\langle \varphi_i \varphi_j | v_{ee} | \varphi_i \varphi_j \rangle - \langle \varphi_j \varphi_i | v_{ee} | \varphi_i \varphi_j \rangle] \quad (2.2.3)$$

h_1 represents for one-electron operator,

$$h_1 = -\frac{1}{2} \nabla_i^2 - \sum_A^M \frac{Z_A}{|r_i - r_A|} \quad (2.2.4)$$

v_{ee} represents for two-electron operator,

$$v_{ee} = \frac{1}{|r_i - r_j|} \quad (2.2.5)$$

Minimizing the HF energy by Lagrange's method of undetermined multipliers, we obtain the HF equations,

$$h_1(x_1)\varphi_i(x_1) + \frac{1}{2} \sum_j^N (u_j(x_1)\varphi_i(x_1) - v_j(x_1)\varphi_i(x_1)) = \varepsilon_i \varphi_i(x_1) \quad (2.2.6)$$

$$u_j(x_1) = \int dx_2 \varphi_j(x_2)^* \frac{1}{|r_i - r_j|} \varphi_j(x_2) \quad (2.2.7)$$

$$v_j(x_1)\varphi_i(x_1) = \int dx_2 \varphi_j(x_2)^* \frac{1}{|r_i - r_j|} \varphi_i(x_2)\varphi_j(x_1) \quad (2.2.8)$$

The term $u_j(x_1)$ is named as the Coulomb operator, which gives the average local potential at point x_1 due to the charge distribution from the electron in orbital φ_j .

Its corresponding term in HF equations is called the Coulomb term, which approximates the Coulomb interaction of an electron in orbital φ_i by counting average effect of the repulsion instead of calculating repulsion interaction explicitly. The orbital describes the behavior of an electron in the net field of all

the other electrons. Here we see in what sense Hartree-Fock is a “mean field” theory.

$$\text{The term } v_j(x_1)\varphi_i(x_1) = \int dx_2 \varphi_j(x_2)^* \frac{1}{|r_i-r_j|} \varphi_i(x_2)\varphi_j(x_1) \quad (2.2.8)$$

is called the exchange term, which has a similar form as the Coulomb term except an exchange of orbital φ_i and φ_j . It arises from the antisymmetry requirement of the wavefunction.

$$f(x_1) = h_1(x_1) + \frac{1}{2} \sum_j^N (u_j(x_1) - v_j(x_1)) \quad (2.2.9)$$

is named as the Fock operator.

As we can see, the HF equations (2.2.6) can be solved numerically. By defining the orbital function as a linear combination of basis functions, we obtain the so called Hartree-Fock-Roothan equations. Then, the orbital equation is solved iteratively with an initial guess for the basis function coefficients until the lowest total energy is reached. For this reason, Hartree-Fock method is called a self-consistent-field (SCF) approach.

2.3 Møller-Plesset Perturbation Theory Second-order Correction

Within HF theory, the probability of finding an electron at some location around an atom is determined by the distance from the nucleus but not the distance to the other electrons. To overcome this limitation, electron correlation is introduced to the original HF method, and we usually call these methods as Post-

HF methods. However, the computational cost of the Post-HF methods is very high and scales prohibitively quickly with the number of electrons treated. One most popular theory is Møller-Plesset perturbation theory (MP).

In MP theory, a small perturbation is added to the usual electronic Hamiltonian H_0 as the electron correlation potential,

$$H = H_0 + V \quad (2.3.1)$$

where

$$V = H_0 - (f + \langle \Psi_0 | H_0 - f | \Psi_0 \rangle) \quad (2.3.2)$$

F is the Fock operator, and the normalized Slater determinant Φ_0 is constructed by the lowest-energy eigenfunction of the Fock operator. MP calculations are not variational. A second-order correction is the most commonly used.

2.4 Coupled Cluster Approximation

Coupled Cluster (CC) approximation is another Post-HF method, and CC is regarded as “the gold standard of quantum chemistry”. The CC wave function is defined by a linear combination of determinants. These determinants are introduced by acting an excitation operator T on the Slater determinant Ψ_0 . Ψ_0 is constructed from HF molecular orbitals,

$$|\Psi\rangle = e^T |\Psi_0\rangle \quad (2.4.1)$$

$$e^T = 1 + T + \frac{T^2}{2!} + \dots \quad (2.4.2)$$

The excitation operator T is defined as

$$T = T_1 + T_2 + T_3 + \dots \quad (2.4.3)$$

where T_1 is the operator of all single excitations, T_2 is the operator of all double excitations and so forth.

CCSD(T) possesses sufficient accuracy to predict the chemical properties of the molecular. However, due to the computational expense, the application of such methods to realistic models is not practical and not likely to become so advances in computer technology.

2.5 Density Functional Theory

Density functional theory (DFT) has become popular in quantum mechanical modeling. This is because the approximate functionals provide a useful balance between accuracy and computational cost, allowing much larger systems to be treated than traditional *ab initio* methods, while retaining much of their accuracy. Nowadays, traditional wavefunction methods, either variational or perturbative, can be applied to calculate highly accurate results on smaller systems, providing benchmarks for developing density functionals, which can then be applied to much larger systems.

As we have discussed above, the wavefunction methods, such as HF and MP2, use the wave function as the central quantity, since it contains the full

information of the many-electron system. However, the wavefunction is a very complicated quantity that cannot be probed experimentally and that depends on $4N$ variables. With the density functional theory, the properties of a many-electron system can be determined by using functional of spatially dependent electron density. In this case, the number of variables is successfully reduced from $4N$ to 3, and incredible speed up the calculation.

As the central quantity in DFT, the electron density is defined as the integral over the spin coordinates of all electrons and over all but one of the spatial variables. It determines the probability of finding any of the N electrons within volume element dr ,

$$\rho(r) = N \int d\sigma dx_2 \cdots dx_N |\Psi(r, \sigma, x_2, \cdots, x_N)|^2 \quad (2.5.1)$$

The wavefunction is normalized,

$$\int dx_1 dx_2 \cdots dx_N |\Psi(r, \sigma, x_2, \cdots, x_N)|^2 = 1 \quad (2.5.2)$$

Thus, the electron density satisfies the equation,

$$\int d^3r \rho(r) = N \quad (2.5.3)$$

The DFT theory is based on two Hohenberg-Kohn theorems: The first Hohenberg-Kohn theorem demonstrates that the electron density uniquely determines the Hamiltonian operator and thus all the properties of the system; The second H-K theorem states that, the functional that delivers the ground state energy of the system, delivers the lowest energy if and only if the input density is the true ground state density. This is nothing but the variational principle.

$$E[\rho] = T[\rho] + E_{int}[\rho] + E_{ext}[\rho] = F_{HK}[\rho] + \int d^3r \rho(r) V_{ext}(r) \quad (2.5.4)$$

$$E_0[\rho_0] = \min_{\rho} (F_{HK}[\rho] + \int d^3r \rho(r) V_{ext}(r)) \quad (2.5.5)$$

Kohn and Sham proposed the following approach to approximating the kinetic and electron-electron functional ²¹. They separated the classical electron-electron Coulomb interaction (Hartree Energy) $E_H[\rho]$ from the $E_{int}[\rho]$,

$$E_H[\rho] = \frac{1}{2} \int d^3r d^3r' \rho(r) \rho(r') \frac{1}{|r-r'|} \quad (2.5.6)$$

At the same time, approximate the kinetic energy by replacing the interaction system with a non-interaction system, while the electron density is kept unchanged,

$$T_{KS} = -\frac{1}{2} \sum_i^N \langle \varphi_i | \nabla^2 | \varphi_i \rangle \quad (2.5.7)$$

$$\rho_{KS}(r) = \sum_i^N \sum_{\sigma} |\varphi_i(r, \sigma)|^2 = \rho(r) \quad (2.5.8)$$

Then, the ground state total energy is represented as:

$$E_{KS}[\rho] = T_{KS}[\rho] + E_H[\rho] + E_{ext}[\rho] + E_{xc}[\rho] \quad (2.5.9)$$

where $E_{xc}[\rho]$, the so-called exchange-correlation energy is defined in this manner,

$$E_{xc}[\rho] = (T[\rho] - T_{KS}[\rho]) + (E_{int}[\rho] - E_H[\rho]) \quad (2.5.10)$$

$E_{xc}[\rho]$ is the sum of the error of the non-interacting kinetic energy approximation and the error of treating the electron-electron Coulomb interaction classically.

Apply the variational principle to the Kohn-Sham energy, we obtain the Kohn-Sham equations,

$$f^{KS}(r)\varphi_i(r) = \left(-\frac{1}{2}\nabla^2 + V_s(r)\right)\varphi_i(r) = \varepsilon_i\varphi_i(r) \quad (2.5.11)$$

$$V_s(r) = \int d^3r' \frac{\rho(r')}{|r-r'|} - \sum_A^M \frac{Z_A}{|r-r_A|} + V_{xc}(r) \quad (2.5.12)$$

The exchange-correlation potential $V_{xc}(r)$, is defined as the functional derivative of $E_{xc}[\rho]$ with respect to ρ ,

$$V_{xc}(r) = \frac{\delta E_{xc}[\rho]}{\delta \rho} \quad (2.5.13)$$

The Kohn-Sham equations result in a quite similar form as the Hartree-Fock equations (2.2.6), and could also be solved iteratively with an initial guess of orbital. The Hartree-Fock equations give accurate exchange potential, while lacking of correlation potential. The Kohn-Sham calculation, which is based on density functional theory (DFT), uses the orbital functions to approximate the true density of the original system. By decoupling the system into a set of single-particle equations, it is much easier to solve than the original problem. By introducing the exchange-correlation potential functional, the Kohn-Sham equations could solve the large system effectively with acceptable sacrifice of accuracy.

How to approximate the exchange-correlation energy exactly is the most challenging part of the problem. In general, there are three kinds of approximations, local density approximation (LDA), semi-local density approximation (GGA), and non-local density approximation (Hybrid)^{22, 23}.

The LDA is only dependent on the information about the density $\rho(r)$ at a particular point r ,

$$E_{xc}^{LDA} = \int d^3r \rho(r) \varepsilon_{xc}(\rho(r)) \quad (2.5.14)$$

The GGA is not only dependent on the local density $\rho(r)$, but also dependent on gradient of the electron density $\rho(r)$ at point r . The typical form of the GGA functional is,

$$E_{xc}^{GGA} = \int d^3r \rho(r) \varepsilon_{xc}(\rho(r), \nabla \rho(r)) \quad (2.5.15)$$

$$E_{xc}^{B3LYP} = a_0 E_x^{HF} + (1 - a_0) E_x^{Slater} + a_x E_x^{Becke88} + (1 - a_c) E_c^{VWN} + a_c E_c^{LYP} \quad (2.5.16)$$

where $a_0 = 0.20$, $a_x = 0.72$, $a_c = 0.81$. The last exchange-correlation potential (2.5.16), which called B3LYP, is a hybrid approximation potential. E_x^{HF} stands for Hartree-Fock exchange energy (third term in (2.2.3)), E_x^{Slater} for Slater exchange energy²⁴, $E_x^{Becke88}$ for the exchange part of Becke88 GGA functional²⁵, E_c^{VWN} for the local Vosko-Wilk-Nusair correlation functional²⁶, and E_c^{LYP} for the correlation part of the Lee-Yang-Parr local and GGA functional²⁷. Due to the accurate approximation of band gaps resulting by B3LYP, we use B3LYP as our exchange-correlation potential when doing all the computations²⁸.

2.6 Linear Combinations of Atomic Orbitals

The method of linear combinations of atomic orbitals (LCAO) is widely used to solve the Kohn-Sham equations. In this approach, we introduce a set of L predefined basis functions $\tau_\beta(r)$ (Further discussed in Section 2.7). The Kohn-Sham orbital is linearly expanded as a combination of $\tau_\beta(r)$,

$$\varphi_i(r) = \sum_{\beta}^L c_{i\beta} \tau_\beta(r) \quad (2.6.1)$$

By multiplying an arbitrary basis function $\tau_\alpha(r)$ from the left side, the Kohn-Sham equations could be simplified to the form,

$$F^{KS} C = S C \epsilon \quad (2.6.2)$$

where C is the coefficient vector $\{c_{i\beta}\}_L$, ϵ is a diagonal matrix of the orbital energies ϵ_i . F^{KS} is called the Kohn-Sham matrix with element $F_{\alpha\beta}^{KS}$,

$$F_{\alpha\beta}^{KS} = \int d^3r \tau_\alpha(r) f^{KS}(r) \tau_\beta(r) \quad (2.6.3)$$

S is the overlap matrix, with element $S_{\alpha\beta}$ defined as,

$$S_{\alpha\beta} = \int d^3r \tau_\alpha(r) \tau_\beta(r) \quad (2.6.4)$$

Both F^{KS} and S are $L \times L$ dimensional. Then, the equations could be solved by standard linear algebra package.

2.7 Local Basis Functions

Two type local basis functions are used for DFT calculation: one is Slater-type-orbitals (STO); the other is Gaussian-type-orbitals (GTO).

STOs are exponential functions that mimic the exact eigenfunctions of the hydrogen atom,

$$\tau^{STO}(r) = Ar^{n-1}\exp[-ar]Y_{lm} \quad (2.7.1)$$

n corresponds to the principal quantum number, the orbital exponent is termed a and Y_{lm} are the usual spherical harmonics. They seem to be the natural choice for basis functions. Unfortunately, many-center integrals are very difficult to compute with STO basis, and they do not play a major role in quantum chemistry.

Gaussian-type-orbitals (GTO) are the usual choice in quantum chemistry. They have the following general form,

$$\tau_i^{GTO}(r) = A_i r^l e^{-\alpha_i f_i^2 r^2} \quad (2.7.2)$$

where A_i is a normalization coefficient, α_i is the exponents, f_i is a scale factor. The contracted Gaussian functions (CGF) basis sets is usually used, in which several primitive Gaussian functions are combined in a fixed linear combination. Then, a single basis function is composed of one or more primitive Gaussian functions,

$$\tau_n^{GTO}(r) = \sum_{i=1}^N d_{in} \tau_i^{GTO}(r) \quad (2.7.3)$$

where N is the number of primitive functions, d_{in} is a coefficient. For any specific basis set, these parameters are predefined and do not change over the course of calculation. An atomic shell is represented through a set of basis functions $\tau_\beta(r)$ with shared exponents

$$\varphi(r) = \sum_\beta c_\beta \tau_\beta(r) = \sum_\beta c_\beta Y_{lm} \tau_n^{GTO}(r) \quad (2.7.4)$$

Usually, an s-shell contains a single s-type basis function; a p-shell contains three basis functions each with symmetry p_x, p_y, p_z ; an sp-shell contains four basis functions s, p_x, p_y, p_z ; A d-shell may contain six functions $d_{x^2}, d_{y^2}, d_{z^2}, d_{xy}, d_{yz}, d_{xz}$, or five functions with symmetry $d_{z^2-r^2}, d_{x^2-y^2}, d_{xy}, d_{yz}, d_{xz}$. Real basis functions are defined by using real angular functions²⁹,

$$S_{lm}^+ = \frac{1}{\sqrt{2}}(Y_{lm} + Y_{lm}^*), \quad S_{lm}^- = \frac{1}{\sqrt{2}i}(Y_{lm} - Y_{lm}^*) \quad (2.7.5)$$

2.8 Time Dependent Density Functional Theory (TDDFT)

TDDFT is an approximate method to solve time dependent Schrödinger equation

$$H\psi = i \frac{\partial}{\partial t} \psi \quad (2.8.1)$$

Similar to DFT, we use Runge-Gross Theorem to solve this equation. By defining an action integral, which is a functional of the time dependent density $\rho(r, t)$,

$$A[\rho] = \int_{t_0}^{t_1} dt \left\langle \psi(r, t) \left| i \frac{\partial}{\partial t} - H[\rho] \right| \psi(r, t) \right\rangle. \quad (2.8.2)$$

In the same manner, we approximate the interaction system with non-interaction orbitals $\varphi_j(r, t), j = 1, \dots, N$, where $\varphi_j(r, t)$ is expanded in the complete space of ground state orbitals $\varphi_k^{gs}(r)$ (both occupied and unoccupied) with a time factor $a_{jk}(t), k = 1, 2, \dots, \infty$. The ground state orbitals $\varphi_j^{gs}(r)$ are used as the initial value of $\varphi_j(r, t)$,

$$\varphi_j(r, t) = \sum_k^\infty a_{jk}(t) \varphi_k^{gs}(r) \quad (2.8.3)$$

$$\varphi_j(r, t_0) = \varphi_j^{gs}(r), j = 1, 2, \dots, N \quad (2.8.4)$$

The time-dependent density $\rho(r, t)$ is kept unchanged for the non-interaction system,

$$\rho(r, t) = \sum_j^N \sum_\sigma |\varphi_j(r, t)|^2 \quad (2.8.5)$$

The time-dependent Kohn-Sham scheme is obtained for the non-interaction orbitals,

$$\left(-\frac{1}{2}\nabla^2 + V_s[\rho](r, t)\right) \varphi_j(r, t) = i \frac{\partial}{\partial t} \varphi_j(r, t) \quad (2.8.6)$$

$$\begin{aligned} V_s[\rho](r, t) &= V_H[\rho](r, t) + V_{ext}(r, t) + V_{xc}[\rho](r, t) \\ &= \int d^3r' \frac{\rho(r', t)}{|r-r'|} - \sum_A^M \frac{Z_A}{|r-r_A|} + V_{xc}^{gs}[\rho(t)](r) \end{aligned} \quad (2.8.7)$$

The time-dependent exchange-correlation potential is approximated by using the ground-state exchange-correlation functional $V_{xc}^{gs}[\rho]$, while the ρ is time dependent.

The orbital equation is solved iteratively to yield the minimum action solution,

$$\frac{\delta A[\rho]}{\delta \rho(r,t)} = 0 \quad (2.8.8)$$

The excitation energies are calculated by linear response theory,

$$\delta \rho(r,t) = \int d^3r' \chi(r,r',t,t') \delta V_{ext}(r',t') \quad (2.8.9)$$

where $\chi(r,r',t,t')$ is the response function derived from perturbation theory.

2.9 Mulliken Population Analysis

A normalized molecular orbital φ of a diatomic molecule can be written in approximate form as a linear combination of normalized Atomic Orbitals φ_r, φ_s of the two respective atoms r and s

$$\varphi = c_r \varphi_r + c_s \varphi_s \quad (2.9.1)$$

The molecular orbital φ is occupied by N electrons. The charge distribution is divided into three parts in space as

$$N\varphi^2 = Nc_r^2\varphi_r^2 + 2Nc_r c_s S_{rs}(\varphi_r \varphi_s / S_{rs}) + Nc_s^2\varphi_s^2 \quad (2.9.2)$$

where S_{rs} is the overlap integral $\int_{\infty} \varphi_r \varphi_s dv$. On integration of each term in above equation over all space, one obtains

$$N = Nc_r^2 + 2Nc_r c_s S_{rs} + Nc_s^2 \quad (2.9.3)$$

According to the distribution, one obtains the atomic distributions N_r and N_s as

$$N_r = Nc_r^2 + Nc_r c_s S_{rs}, \quad N_s = Nc_s^2 + Nc_r c_s S_{rs} \quad (2.9.4)$$

For a general molecular, we obtain the Mulliken population $m_{p,\mu}^i$ in the molecular orbital Ψ_i from the μ th atomic orbital of the p th atom in the same manner

$$m_{p,\mu}^i = N(i)c_\mu^i(c_\mu^i + \sum_{\tau \neq \mu} c_\tau^i S_{\mu,\tau}) \quad (2.9.5)$$

where $N(i)$ represents for the number of electron occupancy in the i th molecular orbital. $N(i)$ is equal to 2 in a closed shell molecule.³⁰

2.10 Gaussian Broadening Approach

The eigenstates are broadened by convolution with the Gaussian function

$$N_{p,\mu}^i(E) = \frac{1}{\sigma\sqrt{\pi}} m_{p,\mu}^i \exp\left(-\frac{(E_i-E)^2}{\sigma^2}\right) \quad (2.10.1)$$

where σ is the broadening parameter, presenting the width of the spectral peak; $m_{p,\mu}^i$ is the Mulliken population in molecular orbital Ψ_i from the μ th atomic orbital of the p th atom.

2.11 Density of States (DOS) and Projected DOS

The total DOS is formulated as

$$N(E) = \sum_p N_p(E) \quad (2.11.1)$$

where $N_p(E)$ is the PDOS in atom p . $N_p(E)$ is given by

$$N_p(E) = \sum_{\mu \in p} N_{p,\mu}(E) = \sum_{\mu \in p} \sum_i N_{p,\mu}^i(E) \quad (2.11.2)$$

where $N_{p,\mu}^i(E)$ is the contribution to the i th molecular orbital from the μ th atomic orbital of the p th atom. $N_{p,\mu}^i(E)$ is obtained by Gaussian broadening approach with the Mulliken population $m_{p,\mu}^i$ as the strength parameter.³¹

2.12 Fermi's Golden Rule

Fermi's Golden Rule is obtained by employing the time-dependent perturbation theory. Start from the time-dependent Schrodinger equation,

$$H\psi = i\hbar \frac{\partial}{\partial t} \psi \quad (2.12.1)$$

where H can be written in the form:

$$H = H_0 + H_I(t) \quad (2.12.2)$$

where H_0 is the Hamiltonian of the unperturbed system, and H_I is a perturbation applied to the system. H_0 satisfies the time independent Schrodinger equation,

$$H_0|\varphi_n\rangle = E_n|\varphi_n\rangle \quad (2.12.3)$$

Then we could present $|\psi(t)\rangle$ by wavefunctions $|\varphi_n\rangle$,

$$|\psi(t)\rangle = \sum_n a_n(t) |\varphi_n\rangle e^{-iE_n t/\hbar} \quad (2.12.4)$$

Insert $|\psi(t)\rangle$ into time dependent Schrodinger equation and project the result on $|\varphi_f\rangle$,

$$\frac{\partial a_f(t)}{\partial t} = \frac{1}{i\hbar} \sum_n \langle \varphi_f | H_I(t) | \varphi_n \rangle a_n(t) e^{i(E_f - E_n)t/\hbar} \quad (2.12.5)$$

In order to solve this equation, we make two assumptions: The system is initially in state $|\varphi_j\rangle$; the perturbation is very weak and applied for a short period of time such that all the coefficients remain nearly unchanged. Then we obtain,

$$\frac{\partial a_f(t)}{\partial t} = \frac{a_j(t)}{i\hbar} \langle \varphi_f | H_I(t) | \varphi_j \rangle e^{i(E_f - E_j)t/\hbar} \quad (2.12.6)$$

$$a_f(t) = \frac{1}{i\hbar} \int_0^t \langle \varphi_f | H_I(t') | \varphi_j \rangle e^{i(E_f - E_j)t'/\hbar} dt' \quad (2.12.7)$$

The above equation holds only for perturbations that last for a very short time and the states of the system are nearly unchanged. Assume $\langle \varphi_f | H_I(t') | \varphi_j \rangle$ is constant over $0 \leq t' \leq t$, and denote

$$H_{fj} = \langle \varphi_f | H_I(t) | \varphi_j \rangle, \quad \Delta = (E_f - E_j)/\hbar \quad (2.12.8)$$

Then

$$a_f(t) = \frac{1}{i\hbar} H_{fj} \int_0^t e^{it'\Delta} dt' \quad (2.12.9)$$

$$a_f(t) \cong \frac{2}{i\hbar\Delta} H_{fj} e^{it'\Delta/2} \sin(t\Delta/2) \quad (2.12.10)$$

The probability of finding the system in the eigenstate $|\varphi_f\rangle$ is $|a_f(t)|^2$, so

$$\begin{aligned} T_{j \rightarrow f} &= \lim_{t \rightarrow \infty} \frac{d|a_f(t)|^2}{dt} = \lim_{t \rightarrow \infty} \left[\frac{d}{dt} \left| \frac{2}{i\hbar\Delta} H_{fj} e^{\frac{it'\Delta}{2}} \sin\left(\frac{t\Delta}{2}\right) \right|^2 \right] \\ &= H_{fj}^2 \left(\frac{2}{\hbar\Delta} \right)^2 \frac{\Delta}{2} \lim_{t \rightarrow \infty} \sin(t\Delta) = H_{fj}^2 \left(\frac{2}{\hbar\Delta} \right)^2 \frac{\Delta}{2} \pi \Delta \lim_{t \rightarrow \infty} \frac{\sin(t\Delta)}{\pi\Delta} \\ &= H_{fj}^2 \left(\frac{2\pi}{\hbar^2} \right) \delta(\Delta) = \frac{2\pi}{\hbar} H_{fj}^2 \delta(\hbar\Delta) = \frac{2\pi}{\hbar} |\langle \varphi_f | H_I(t) | \varphi_j \rangle|^2 \delta(E_f - E_j) \end{aligned} \quad (2.12.11)$$

Chapter 3

Computational Model

3.1 Design of Simulation Model

Four sizes of Cd_nSe_n QDs have been considered for our investigation, with ‘n’ = 6, 12, 13, and 33. They were cut directly from the CdSe würtzite bulk crystal³². These CdSe QDs have been intensively studied both theoretically and experimentally¹³⁻¹⁷. Cd_6Se_6 , $\text{Cd}_{13}\text{Se}_{13}$, and $\text{Cd}_{33}\text{Se}_{33}$ are ‘magic size’ QDs; $\text{Cd}_{33}\text{Se}_{33}$ has been synthesized experimentally³³. The four capping ligands contain a sulfur group and terminate with the carboxyl group (e.g. HS-R-COOH). This family is commonly used to saturate CdSe QDs, as has been done with other ligand families, based upon analogous NH_3 , PH_3 , and OPH_3 groups.

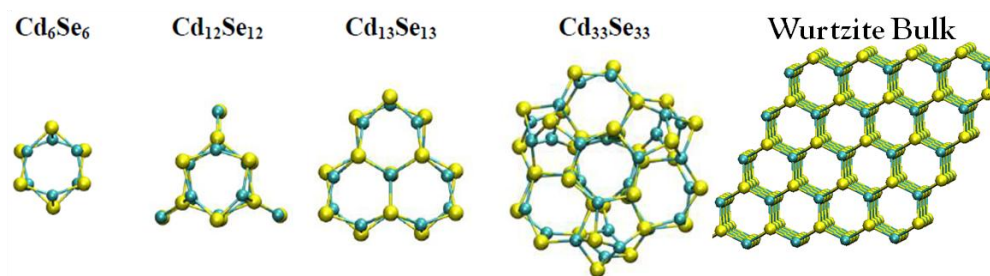


Figure 3.1: Structures of Four Sizes CdSe Quantum Dots and Crystal Bulk (Cd: cyan, Se: yellow)

We have introduced two control parameters amongst these four ligands: one parameter either the presence or absence of NH₂ in the ‘R’ functional chain, such as Cys vs. MPA; the other parameter involves varying the length of the ‘R’ chain, such as Cys vs. HSCH(NH₂)COOH. We have studied the effects of these two parameters on the structure and optical properties of CdSe QDs. According to the experimental results^{6,10}, the sulfur group possesses a high affinity for the Cd atom. Here, we pursue an approach similar to reference¹⁴ in order to functionalize the surface, with the ligands strongly bonded to Cd atoms with two dangling bonds.

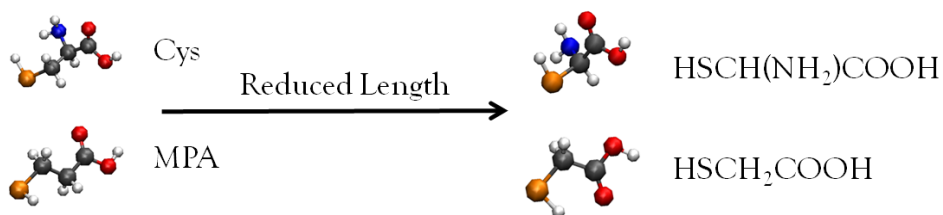


Figure 3.2: Structures of MPA and Cys and Their Reduced Chain Analogy (S: orange, N: blue, C: gray, O: red, H: white)

3.2 Simulation Methodology

All of our calculations were performed on NWCHEM 6.0 program³⁴. The basis sets, LANL2DZ³⁵ and 6-31G*^{36, 37} have been employed for CdSe and

ligands, respectively. This choice of basis sets has proved to be a pragmatic but sufficient balance between the accuracy and computational intensity³⁸. Both PBE^{39, 40} and B3LYP⁴¹ exchange and correlation (XC) functionals have been applied for DFT geometry optimization, whereas the TDDFT calculation is based on the B3LYP XC functional. These two functional theories have been commonly used to study CdSe QDs^{14, 17, 18, 42}. In order to reduce the energy state degeneracy, the symmetry is suppressed during the simulation. This choice has been verified in previous work¹⁶⁻¹⁸. The Visual Molecular Dynamics software (VMD)⁴³ has been used for structure visualization.

3.3 Geometry Optimization of QDs

The geometry optimization is employed on the raw CdSe quantum dots. The structure is relaxed until a minimum-energy configuration is reached,

$$F(R) = -\frac{\partial E(R)}{\partial R} = 0 \quad (3.3.1)$$

where R is the degrees of freedom. In our case, R represents for the vector composed by the bond lengths and angles of the molecular structure. When doing the optimization, the Quasi-Newton method is applied to search the optimized structure,

$$f(x + \Delta x) = f(x) + \nabla f(x)^T \Delta x + \frac{1}{2} \Delta x^T B \Delta x \quad (3.3.2)$$

where B is the Hessian Matrix. For each step in the optimization, the total energy is calculated by DFT.

3.4 Verification and Validation of Simulation

Here we duplicate prior results in order to verify the correctness and plausibility of our approach and method. The average bond length of optimized Cd_6Se_6 has been computed to be 2.699 Å / 2.862 Å for intra/inter layer Cd-Se (Table 3.1) by using the LANL2DZ basis sets and B3LYP functional. These data are consistent with the results of P. Yang¹⁷ and A. Kuznetsov¹⁸. The band gap values for Cd_6Se_6 and $\text{Cd}_{13}\text{Se}_{13}$ obtained by using the B3LYP functional are 3.14 eV and 3.06 eV, respectively, which are in good agreement with earlier results^{17, 18, 44}. As shown in Table 3.1, less than 1% difference to the reference data¹ for bond length and energy gap is obtained by our calculation, which is in the tolerance of the error for simulation.

The absorption peak for Cys capped $\text{Cd}_{33}\text{Se}_{33}$ is estimated from 2.7 ~ 3.0 eV, which is equivalent to 413 ~ 460 nm. The experimental observed absorption peak of 2nm Cys-capped CdSe QDs is reported as 422nm¹⁰, which is consistent with our estimation. Section 4.3 will have a detailed discussion for this part.

Table 3.1: Comparing Results of Bond Length and Energy Gap with Reference Data (in the parentheses). All the calculation is using LANL2DZ basis set and B3LYP exchange and correlation functional.

System	Cd-Se Bond Length (Å) (intra / inter layer)	HOMO-LUMO Gap (eV)
Cd_6Se_6	2.699 / 2.862 (2.670 / 2.864)	3.14 (3.14)
$\text{Cd}_{13}\text{Se}_{13}$	2.710 / 2.801 (2.704 / 2.785)	3.06 (2.99)

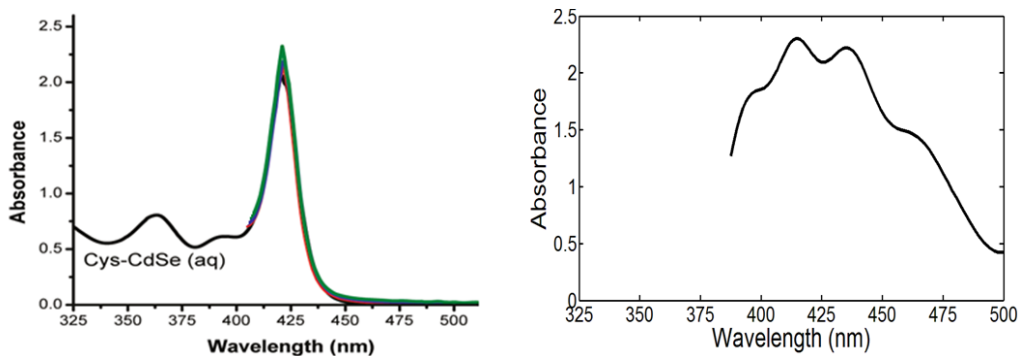


Figure 3.3: Absorption Peak of Cys-capped $\text{Cd}_{33}\text{Se}_{33}$. Left: Experimental result ¹⁰; Right: Simulation Estimation.

Chapter 4

Simulation Results

4.1 Bare Quantum Dots

In this section, we carry out a comparison between ‘magic’ and ‘non-magic’ size quantum dots. In doing so, we explore the disadvantages of the ‘non-magic’ size dots. The geometrically optimized coordinates of the bare Cd_nSe_n QDs ($n = 6, 12, 13,$ and 33) have been calculated. The visualization of the cluster is provided in Table 4.1. The geometry optimization leads to a surface reconstruction of the large bare quantum dots, while the core wurtzite structure is maintained. As compared with the values for the other three sizes of QDs, $\text{Cd}_{12}\text{Se}_{12}$ possesses a smaller HOMO-LUMO gap of 2.08 eV (Figure 4.1(a), Table A. 1). The calculated binding energy per Cd-Se pair of $\text{Cd}_{12}\text{Se}_{12}$ is also smaller than the other sized particles (Figure 4.1(a)). In previous work by other groups, the Cd_nSe_n clusters with $n = 6, 13,$ and 33 have been observed to be ultra-stable structures⁴⁴⁻⁴⁶ with high binding energy per atom. The surface Cd and Se atoms are all three-coordinated atoms for relaxed ‘magic size’ QDs, whereas $\text{Cd}_{12}\text{Se}_{12}$ still retains several two-coordinated atoms. These two-coordinated atoms generate trap states inside the band gap (Figure 4.1(b)). This result is consistent with previous theoretical and experimental studies of small-sized CdSe clusters^{45, 47, 48}.

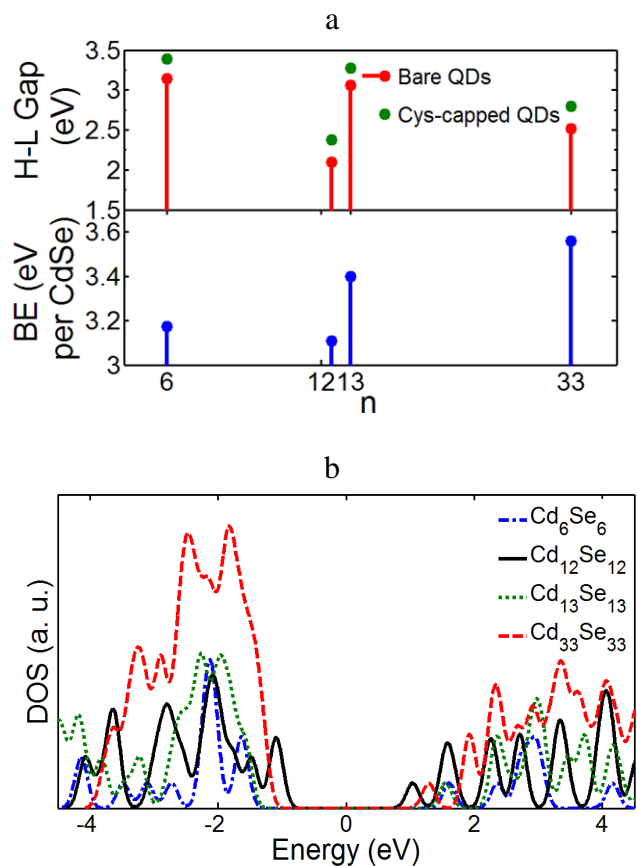


Figure 4.1. (a) Band gap value and binding energy per Cd-Se pair and (b) Density of states (DOS) of different size bare Cd_nSe_n QDs ('n' = 6, 12, 13, and 33) calculated using the B3LYP / LANL2dz methodology. The Fermi energy has been chosen to be in the middle of the HOMO-LUMO gap and a Gaussian broadening of 0.1 eV has been used for the DOS calculations in (b).

4.2 Quantum Dots Capped by Organic Ligands

We discuss the structure and HOMO-LUMO gap of the capped CdSe QDs in this section. The optimized structures of the capped Cd_nSe_n QDs ($n = 6, 12, 13, \text{ and } 33$) are documented in Table 4.1, while the bond length, the binding energy, and the HOMO-LUMO gap are documented in Table 4.2. Two XC functionals, PBE and B3LYP, show the same trend in all of the species tested (Table A. 2). As we have discussed in Section 4.1, use of the B3LYP functional results in a quantitatively better description for the bond length and a closer fit to experimental work than analogous use of the PBE functional. Thus, all of our later discussion is based on the geometry relaxed by using the B3LYP functional.

When Cd_nSe_n is capped by organic ligands, the structure of CdSe QD is slightly perturbed after the geometry optimization (Table 4.2). For Cd_6Se_6 , the inter layer Cd-Se bond adjacent to the ligand is elongated and the one furthest from the ligand is shortened. For $\text{Cd}_{12}\text{Se}_{12}$, $\text{Cd}_{13}\text{Se}_{13}$, $\text{Cd}_{33}\text{Se}_{33}$, the surface Cd-Se bond length is slightly elongated and the core length is shortened. The only exception is the core interlayer bond length of capped $\text{Cd}_{33}\text{Se}_{33}$, which is also elongated by the ligands. We conclude that adding the surfactant tends to weaken the surface Cd-Se bonds and strengthen the core Cd-Se bonds. When the diameter of the CdSe QD increases, the core of the quantum dot is more likely to be preserved whereas the ligands reposition the surface atoms of the CdSe QDs.

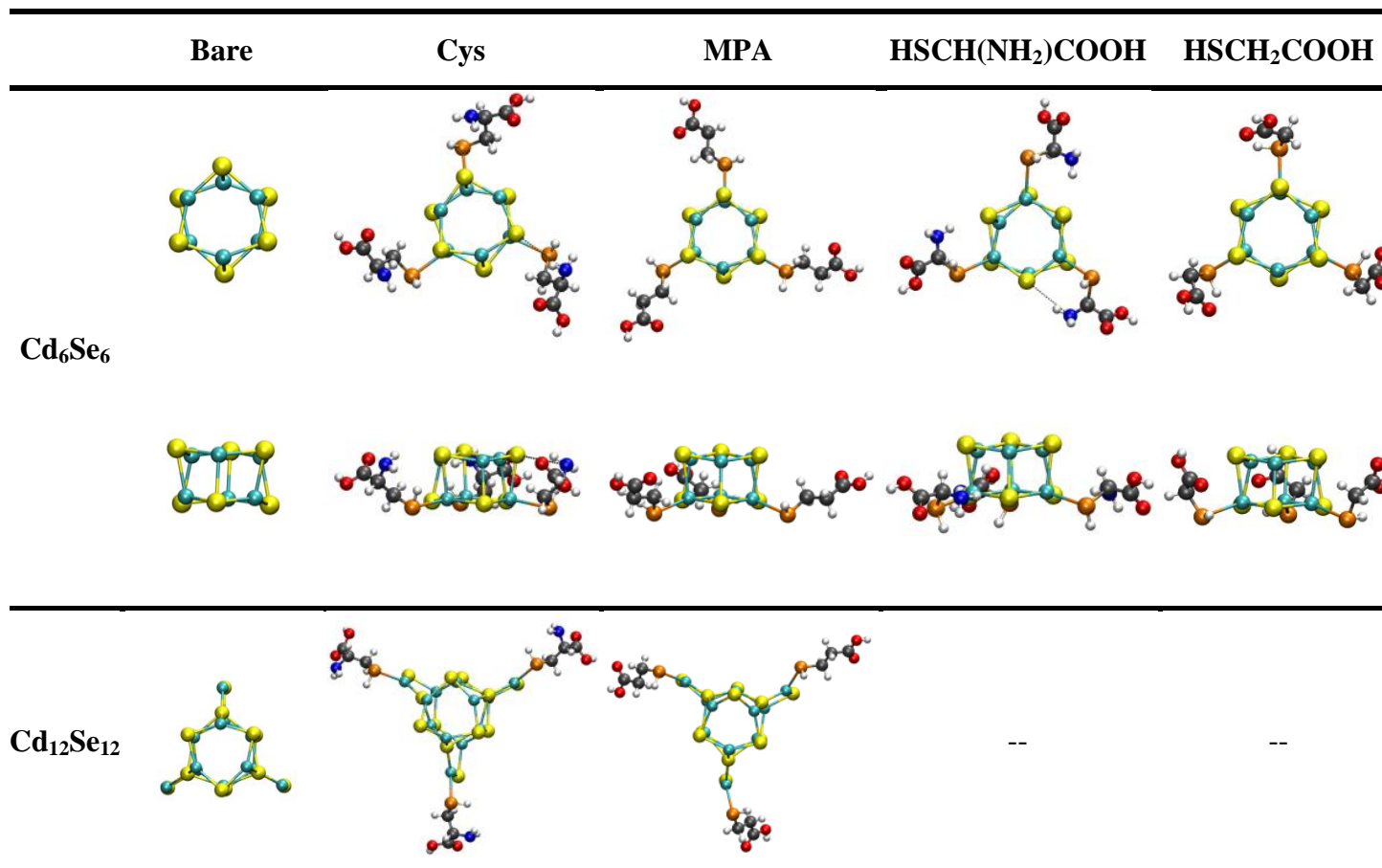
Besides the effects on the structure of QDs, the ground state HOMO-LUMO gaps also possess an increase of 0.2 ~ 0.3 eV (Table 4.2) from the bare QDs when capped by the ligands. As we have discussed in Section 4.1, the HOMO-LUMO gap value is decreased when increasing the size of QD, except for Cd₁₂Se₁₂: Cd₁₂Se₁₂ possesses an abnormally smaller band gap. This result is consistent with the quantum confinement effect that has been observed for semiconductors¹¹. When the QDs are passivated by the organic ligands, the trend of band gap value of different size QDs is preserved (Figure 4.1(a)). Compared with the magic size QDs, the saturated non-magic size Cd₁₂Se₁₂, still preserves an abnormally smaller band gap. Thus, the ligand passivation does not fundamentally stabilize the structure and improve the optical property of non-magic size QD. A deeper analysis of the absorption properties of the capped QDs is presented in Section 4.3.

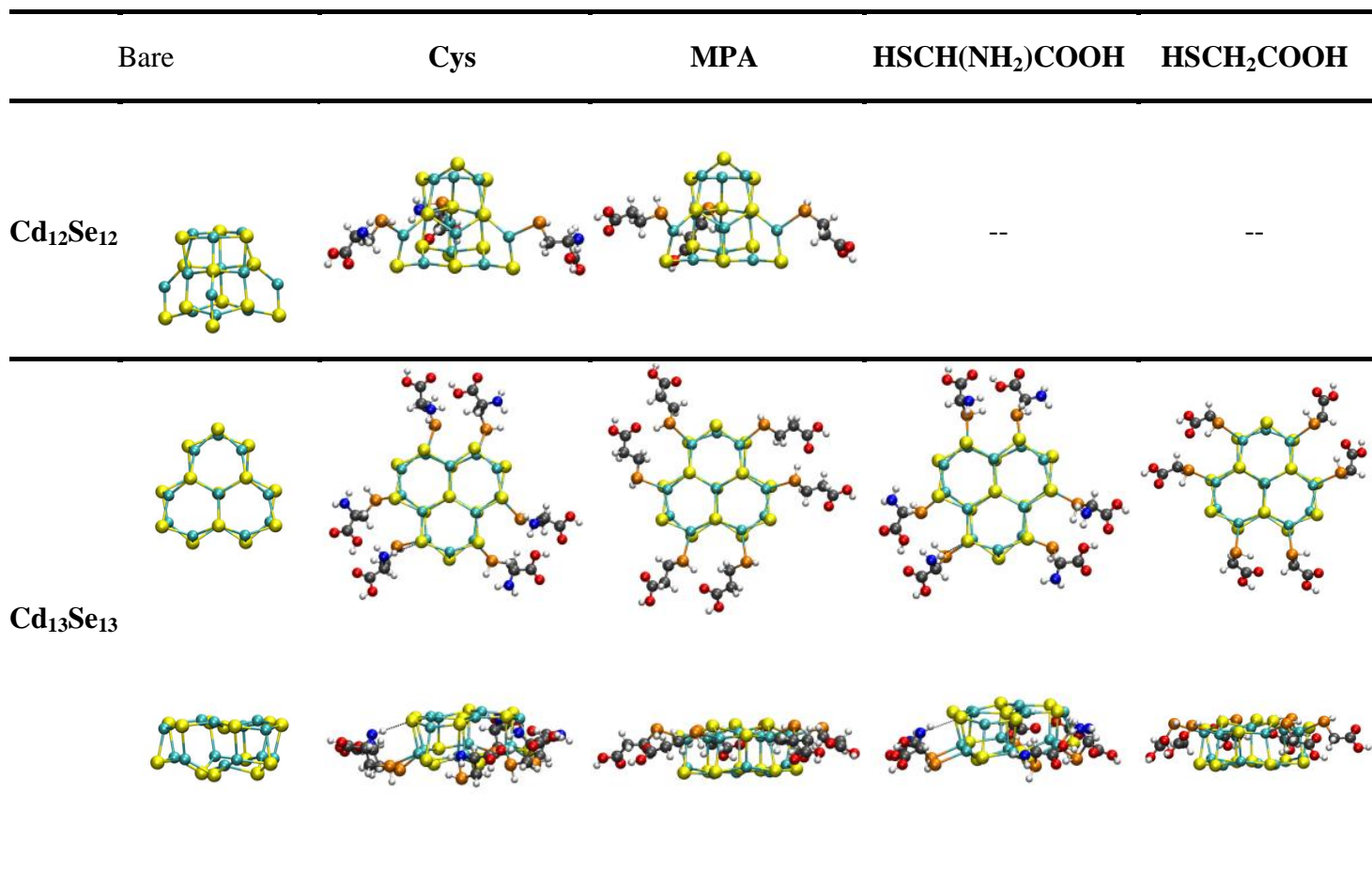
Unlike the significant difference between bare QDs and capped ones, only a minor perturbation is observed in the structure and band gap values between QDs capped with Cys and MPA, respectively, as well as for different length ligands. As shown in Table 4.2 (Table A. 2), the amine group of HSCH(NH₂)COOH tends to move closer to the neighboring Se atom than does the Cys, as a result of the shorter alkane chain. An enhancement of the binding energy between the Cd atom and the ligand is also observed from

HSCH(NH₂)COOH to Cys. For the MPA and HSCH₂COOH capped QDs, no distinct difference as same as HSCH(NH₂)COOH and Cys is observed.

As we have observed, both involving the amine group and shortening the length of 'R' chain have only a minor effect on the electronic properties of the CdSe QDs. As long as the ligands are in the thiol category, an increase of HOMO-LUMO gap by about ~0.28 eV is obtained by the passivation. In reference ¹⁴, with a same approach to saturate the Cd₃₃Se₃₃ and calculate the band gap, increases of ~0.14 eV and of ~0.19 eV are reported for Cd₃₃Se₃₃ coated by OPMe₃ and NH₂Me, respectively. The thiol category ligand might possess a better ability to open the band gap of CdSe QD than amine or phosphine oxide ligands.

Table 4.1. Optimized structures of Cd_nSe_n + Ligands ('n' = 6, 12, 13, and 33) using the B3LYP functional theory with the LANL2DZ/6-31G* (CdSe/Ligand) basis sets (Cd: cyan, Se: yellow, H: white, S: orange, C: gray, O: red, N: blue).





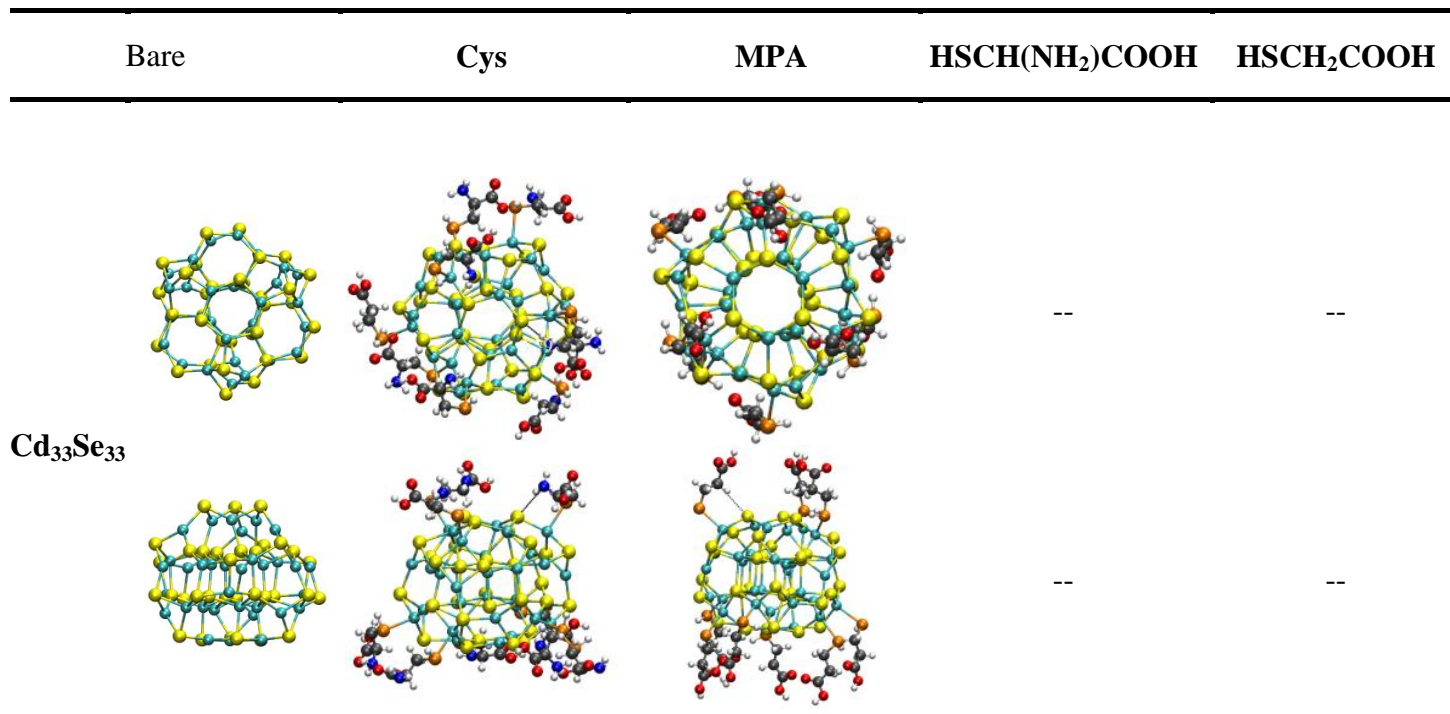


Table 4.2. Species of Cd_nSe_n ('n' = 6, 12, 13, 33) + Ligands calculated using B3LYP functional with LANL2DZ/6-31G* (CdSe/Ligand) basis sets.

System	Ligands	Bond Length (Å)		Distance of N-Se (Å)	BE of Cd-L (kcal/mol)	H-L Gap (eV)
		Cd-Se (intra(c)/intra(s)/inter(c)/inter(s))				
Cd ₆ Se ₆ ¹	Bare	2.699/ -- /2.862/ --		--	--	3.14
	Cys	2.693/2.717/2.828/2.950		2.876	4.05	-10.612
	MPA	2.696/2.720/2.820/2.926		2.795	--	-11.538
	HSCH(NH₂)COOH	2.693/2.733/2.821/2.913		2.846	3.71	-13.190
	HSCH₂COOH	2.698/2.723/2.807/2.936		2.858	--	-12.213
Cd ₁₂ Se ₁₂	Bare	2.972/2.703/2.806/2.535		--	--	2.10
	Cys	2.929/2.705/2.768/2.558		2.874	3.79	-12.179
	MPA	2.930/2.708/2.765/2.556		2.895	--	-9.039

¹ The Cd-Se bond length of ligated Cd₆Se₆ is classified as “**intra/intra(L)/inter/inter(L)**”, representing for intra layer bond, intra layer bond adjacent to the ligand, inter layer bond and inter layer bond adjacent to ligand, respectively.

System	Ligands	Bond Length (Å)		Distance of N-Se (Å)	BE of Cd-L (kcal/mol)	H-L Gap (eV)
		Cd-Se (intra(c)/intra(s)/inter(c)/inter(s))	Cd-L			
Cd₁₃Se₁₃	Bare	2.778/2.693/3.102/2.801	--	--	--	3.06
	Cys	2.764/2.705/3.050/2.822	2.908	3.78	-11.157	3.27
	MPA	2.773/2.699/3.034/2.843	2.885	--	-11.763	3.26
	HSCH(NH₂)COOH	2.755/2.702/3.046/2.845	2.856	3.67	-14.446	3.28
	HSCH₂COOH	2.765/2.700/3.046/2.840	2.885	--	-11.999	3.25
Cd₃₃Se₃₃	Bare	2.869/2.732/2.730/2.756	--	--	--	2.52
	Cys	2.804/2.763/2.955/2.802	2.874	3.79	-12.179	2.80
	MPA	2.800/2.758/2.949/2.814	2.895	--	-9.039	2.79

4.3 Optical Properties of QDs

We extend the results of Section 4.2 with a deeper analysis of the optical properties of QDs based on the ground states (DFT) and the excited states properties (TDDFT).

To analyze the effects of capping with different ligands, we decomposed the states close to the frontier orbitals of bare and capped QDs identifying DOS peaks with specific electron states of specific atoms. Figure 4.2 is an example for the case of Cd_6Se_6 . Only orbital compositions with larger than 10% contribution were labeled in Figure 4.2. The dominant contribution to the orbitals close to the HOMO and LUMO states originate from the CdSe quantum dot as opposed to the surface ligands on the surface-capped structures. The orbitals of the ligand atoms are localized deep inside the valence band and conduction band (Figure 4.2). This observation coincides with the results of reference ¹⁶. When the CdSe structure is saturated by the organic ligands, the DOS of the Cd and Se orbitals are increased near the HOMO and LUMO area, respectively, and a small open of the gap is observed. This results in a narrower and more intensive absorption peak from bare to capped QDs (Figure 4.3 (a)).

In Table 4.3, we demonstrate the decomposition of dominant excited states of the first and second peaks of the absorption spectrum, as results from a TDDFT calculation. We characterize these excitations by looking at the occupied and

unoccupied states involved in the transitions. As we can see, almost all the involved orbitals which possess dominant contributions to the absorption peaks are localized on the CdSe QDs. This observation agrees well with Kilina's work¹⁴. This observation could therefore explain the relatively minor influence of different ligands upon the observed absorption spectrum; even though the DOS of Cys and MPA capped QDs are actually quite different (Figure 4.2). Furthermore, for bare and capped QDs, all the transitions are occurred among certain orbitals (Table 4.3) with close isosurface patterns of wavefunction (Table 4.4). For instance, as shown in Table 4.3, all the first peaks are excited from HOMO-2 states to LUMO states, no matter the QD is bare or capped by certain ligands. The isosurface of HOMO² and LUMO possess almost identical pattern from bare Cd₁₃Se₁₃ to capped ones, respectively (Table 4.4). The surfactants shift the excitations to a higher energy by ~0.2 eV without generating new excitation channels.

For the capped Cd₃₃Se₃₃, the TDDFT calculation is computationally too intensive to perform. According to the above conclusion, the surfactants induce a blue shift of the absorption peak by ~0.2 eV from the bare QD with a doubled intensity and a narrower half-width. This inference offers a feasible approach to estimate the absorption peak of the capped Cd₃₃Se₃₃ QDs by shifting the spectrum

² Since the HOMO, HOMO-1, and HOMO-2 states are degenerated, we uniformly plot out the isosurface of the wavefunction for HOMO state for analysis.

of bare QD. In order to assess this approach, we compare the approximate peak value with experiment. As shown in Figure 4.3, two absorption peaks are observed by the calculation, whereas the second absorption peak is about 3-fold more intensive than the first peak. According to the judgment in Ref ⁴⁹, the first allowed excitation corresponding to HOMO-LUMO gap might too weak to be detected experimentally, and the second absorption peak is commonly regarded as the correspondence to the experimental absorption peak. For the bare Cd₃₃Se₃₃, the second absorption peak is localized around 2.5 ~ 2.8 eV. Thus, the absorption peak for Cys capped Cd₃₃Se₃₃ is probably valued from 2.7 ~ 3.0 eV, which is equivalent to 413 ~ 460 nm. The experimental observed absorption peak of 2nm Cys-capped CdSe QDs is reported as 422nm ¹⁰, which is consistent with our estimation.

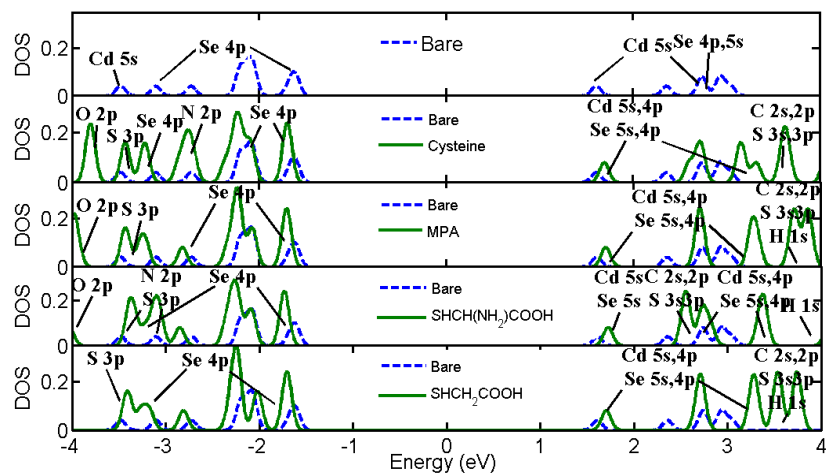


Figure 4.2. Density of states (DOS) of Cd_6Se_6 with four ligands calculated using the B3LYP / (LANL2dz/6-31G*) method. The Fermi energy is set in the middle of the HOMO-LUMO gap, and a Gaussian broadening of 0.05 eV has been used for the DOS calculations.

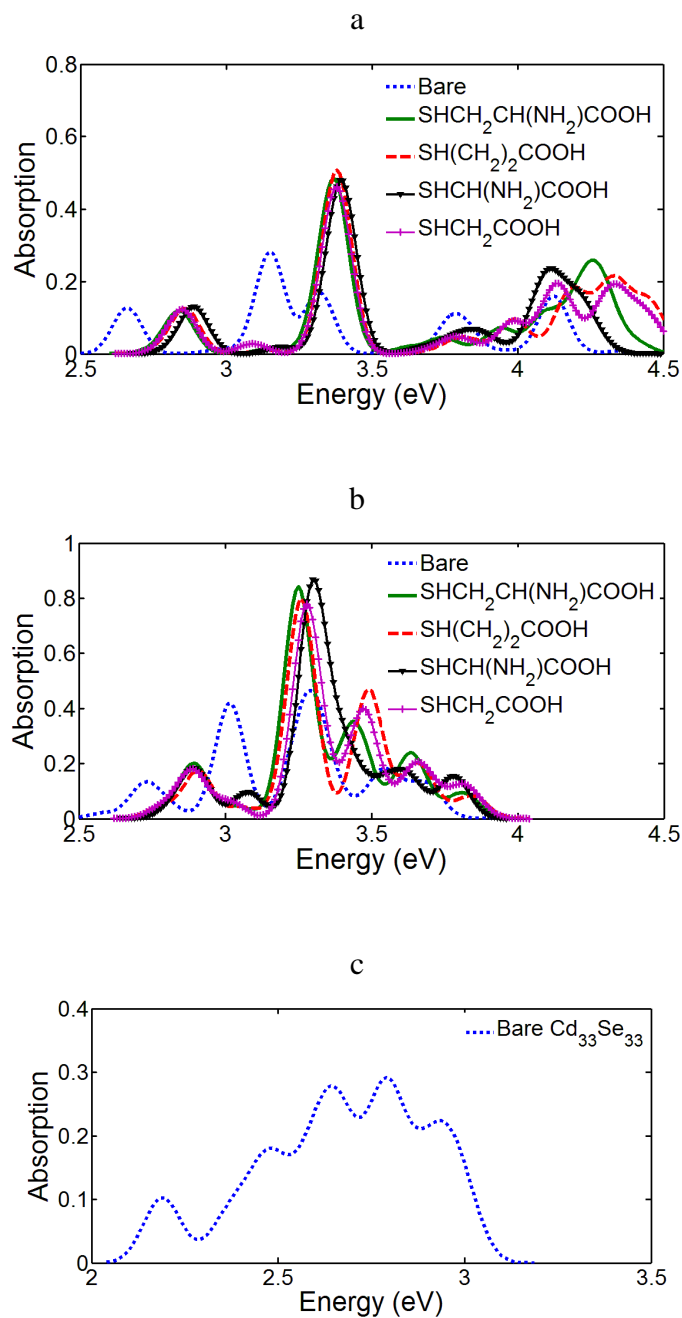


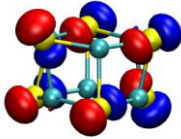
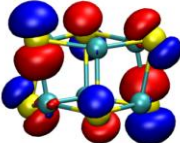
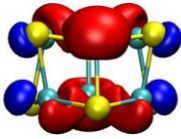
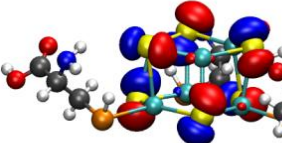

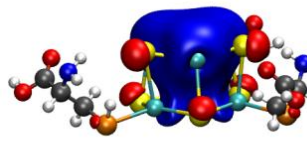
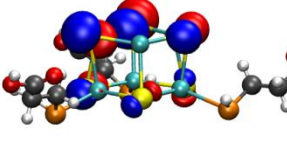
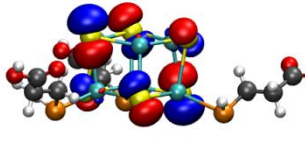
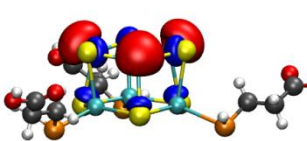
Figure 4.3. Absorption spectra for (a) Cd_6Se_6 with four different ligands, (b) $\text{Cd}_{13}\text{Se}_{13}$ with four different ligands, (c) bare $\text{Cd}_{33}\text{Se}_{33}$. The B3LYP / (LANL2dz/6-31G*) method is used for the TDDFT calculation. A Gaussian broadening of 0.05 eV has been used.

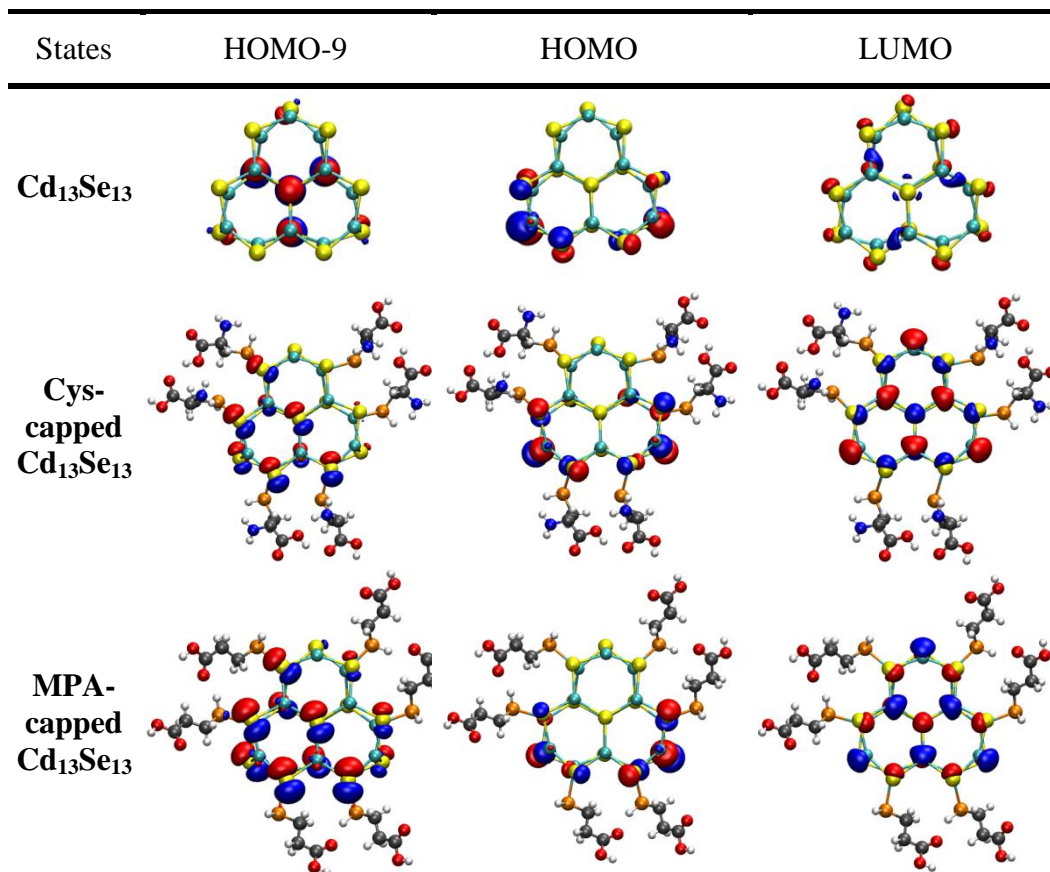
Table 4.3. Decomposition of the representative TDDFT excited-states of Cd_nSe_n ('n' = 6, 13) with four ligands and bare $\text{Cd}_{33}\text{Se}_{33}$. A full list of transition states of capped Cd_6Se_6 is in Table A. 3.

System	Ligands	State Index	Energy (eV)	Oscillator Strength	Excited-State Composition
Cd_6Se_6	--	3	2.66	0.0684	97% H-2 (Se 4p) — L (Cd 5s, Se 5s)
		9	3.15	0.0768	61% H-7 (Se 4p) — L
	Cys	3	2.84	0.0635	84% H-2 (Se 4p) — L (Cd 5s, Se4p)
		8	3.37	0.1294	55% H-7 (Se 4p) — L
	MPA	3	2.86	0.0673	96% H-2 (Se 4p) — L (Cd 5s, Se 5s)
		9	3.38	0.1362	85% H-5 (Se 4p) — L
	SHCH(NH ₂)COOH	3	2.89	0.0682	96% H (Se 4p) — L (Cd 5s, Se 5s)
		9	3.40	0.1059	69% H-5 (Se 4p) — L
	SHCH ₂ COOH	3	2.85	0.0649	96% H-2 (Se 4p) — L (Cd 5s, Se 5s)
		9	3.38	0.1219	47% H-6 (Se 4p) — L
					40% H-7 (Se 4p) — L

System	Ligands	State Index	Energy (eV)	Oscillator Strength	Excited-State Composition
Cd₁₃Se₁₃	--	3	2.72	0.0637	96% H-2 (Se 4p) — L (Cd 5s, Se 5s)
		10	3.02	0.1042	90% H-9 (Se 4p) — L
	Cys	5	2.90	0.0865	96% H-2 (Se 4p) — L (Cd 5s, Se4p)
		10	3.25	0.2272	92% H-9 (Se 4p) — L
	MPA	5	2.91	0.0846	97% H-2 (Se 4p) — L (Cd 5s, Se 5s)
		11	3.26	0.2162	92% H-9 (Se 4p) — L
	SHCH(NH₂)COOH	5	2.90	0.0808	95% H-2 (Se 4p) — L (Cd 5s, Se 5s)
		11	3.30	0.2276	92% H-9 (Se 4p) — L
	SHCH₂COOH	5	2.89	0.0852	97% H-2 (Se 4p) — L (Cd 5s, Se 5s)
		11	3.28	0.2097	91% H-9 (Se 4p) — L
Cd₃₃Se₃₃	--	1	2.19	0.0276	97% H (Se 4p) — L (Cd 5s, Se 5s)
		8	2.46	0.0411	94% H-7 (Se 4p) — L
		17	2.67	0.0667	79% H-16 (Se 4p) — L
		25	2.79	0.0341	67% H-22 (Se 4p) — L

Table 4.4. The isosurface of wavefunction superimposed on the atomic structure of bare and capped QDs. The selected states are all active in the excitation as shown in Table 4.3.

States	HOMO-7	HOMO	LUMO
Cd_6Se_6			
Cys-capped Cd_6Se_6			
MPA-capped Cd_6Se_6			



Chapter 5

Conclusions

In this work, we have performed a first-principles study of small Cd_nSe_n QDs ('n' = 6, 12, 13, and 33) with two different types of ligands and their reduced-chain analogues. The major conclusions from the dissertation are as follows: When the QDs capped by surface ligands, the structure of CdSe QD is well preserved. The surface Cd-Se bonds are slightly weakened whereas the core bonds are strengthened. A blue shift of the absorption peak by ~0.2 eV has been observed from bare to capped QDs. Besides the value shift, the ligated dots exhibit narrower and more intensive optical absorption peaks. By contrast, we have observed that both involving the amine group in the 'R' chain and varying the length of 'R' chain yield only a minor effect upon the absorption properties, though a shorter alkane chain might induce a slightly stronger interaction between the $-\text{NH}_2$ group and the nearest surface Se atom, which is observed as a stronger ligand binding energy.

We also confirm that use of the B3LYP functional results in a quantitatively better description for the bond length and a closer fit to experimental work than analogous use of the PBE functional. The ligand passivation does not fundamentally stabilize the structure and improve the optical

property of non-magic size QD. When compared to amine or phosphine oxide ligands, the thiol category ligand possesses a better ability to open the band gap of CdSe QDs.

Bibliography

1. Cho, A., *Energy's Tricky Tradeoffs*. Science, 2010. **329**(5993): p. 786-787.
2. *Renewables 2011 Global Status Report*. REN21, 2011: p. 17-18.
3. *Paper to WREC X 2008*, SUNA Iran.
4. Kongkanand, A., et al., *Quantum Dot Solar Cells. Tuning Photoresponse through Size and Shape Control of CdSe–TiO₂ Architecture*. J. Amer. Chem. Soc., 2008. **130**(12): p. 4007-4015.
5. Murray, C.B., D.J. Norris, and M.G. Bawendi, *Synthesis and characterization of nearly monodisperse CdE (E = sulfur, selenium, tellurium) semiconductor nanocrystallites*. J. Amer. Chem. Soc., 1993. **115**(19): p. 8706-8715.
6. Robel, I., et al., *Quantum Dot Solar Cells. Harvesting Light Energy with CdSe Nanocrystals Molecularly Linked to Mesoscopic TiO₂ Films*. J. Amer. Chem. Soc., 2006. **128**(7): p. 2385-2393.
7. Guijarro, N., et al., *CdSe Quantum Dot-Sensitized TiO₂ Electrodes: Effect of Quantum Dot Coverage and Mode of Attachment*. J. Phys. Chem. C, 2009. **113**(10): p. 4208-4214.
8. Sambur, J.B., et al., *Influence of Surface Chemistry on the Binding and Electronic Coupling of CdSe Quantum Dots to Single Crystal TiO₂ Surfaces*. Langmuir, 2010. **26**(7): p. 4839-4847.
9. Bang, J.H. and P.V. Kamat, *Solar Cells by Design: Photoelectrochemistry of TiO₂ Nanorod Arrays Decorated with CdSe*. Adv. Funct. Mater., 2010. **20**(12): p. 1970-1976.
10. Nevins, J.S., K.M. Coughlin, and D.F. Watson, *Attachment of CdSe Nanoparticles to TiO₂ via Aqueous Linker-Assisted Assembly: Influence of Molecular Linkers on Electronic Properties and Interfacial Electron Transfer*. ACS Appl. Mater. Interfaces, 2011. **3**(11): p. 4242-4253.
11. Jasieniak, J., M. Califano, and S.E. Watkins, *Size-Dependent Valence and Conduction Band-Edge Energies of Semiconductor Nanocrystals*. ACS Nano, 2011. **5**(7): p. 5888-5902.

12. Park, Y.-S., et al., *Size-Selective Growth and Stabilization of Small CdSe Nanoparticles in Aqueous Solution*. ACS Nano, 2009. **4**(1): p. 121-128.
13. Puzder, A., et al., *Self-healing of CdSe nanocrystals: first-principles calculations*. Phys. Rev. Lett., 2004. **92**(21): p. 217401-217404.
14. Kilina, S., S. Ivanov, and S. Tretiak, *Effect of Surface Ligands on Optical and Electronic Spectra of Semiconductor Nanoclusters*. J. Amer. Chem. Soc., 2009. **131**(22): p. 7717-7726.
15. Schapotschnikow, P., B. Hommersom, and T.J.H. Vlugt, *Adsorption and Binding of Ligands to CdSe Nanocrystals*. J. Phys. Chem. C, 2009. **113**(29): p. 12690-12698.
16. Del Ben, M., et al., *Density Functional Study on the Morphology and Photoabsorption of CdSe Nanoclusters*. J. Phys. Chem. C, 2011. **115**(34): p. 16782-16796.
17. Yang, P., S. Tretiak, and S. Ivanov, *Influence of Surfactants and Charges on CdSe Quantum Dots*. J. Clust. Sci., 2011. **22**(3): p. 405-431.
18. Kuznetsov, A.E., et al., *Structural and Electronic Properties of Bare and Capped Cd_nSe_n/Cd_nTe_n Nanoparticles (n = 6, 9)*. J. Phys. Chem. C, 2012. **116**: p. 6817-6830.
19. Xu, S.H., C.L. Wang, and Y.P. Cui, *Theoretical investigation of CdSe clusters: influence of solvent and ligand on nanocrystals*. J. Mol. Model., 2010. **16**(3): p. 469-473.
20. Chung, S.-Y., et al., *Structures and Electronic Spectra of CdSe–Cys Complexes: Density Functional Theory Study of a Simple Peptide-Coated Nanocluster*. J. Phys. Chem. B, 2008. **113**(1): p. 292-301.
21. Kohn, W. and L.J. Sham, *Self-Consistent Equations Including Exchange and Correlation Effects*. Physical Review, 1965. **140**(4A): p. A1133-A1138.
22. Burke, K., *The ABC of DFT*. 2003.
23. Saad, Y., J.R. Chelikowsky, and S.M. Shontz, *Numerical Methods for Electronic Structure Calculations of Materials*. SIAM Review, 2010. **52**(1): p. 3-54.

24. Slater, J.C. and K.H. Johnson, *Self-Consistent-Field X α Cluster Method for Polyatomic Molecules and Solids*. Physical Review B, 1972. **5**(3): p. 844-853.
25. Becke, A.D., *Density-functional exchange-energy approximation with correct asymptotic behavior*. Physical Review A, 1988. **38**(6): p. 3098-3100.
26. Vosko, S.H., L. Wilk, and M. Nusair, *Accurate spin-dependent electron liquid correlation energies for local spin density calculations: a critical analysis*. Canadian Journal of Physics, 1980. **58**(8): p. 1200-1211.
27. Lee, C., W. Yang, and R.G. Parr, *Development of the Colle-Salvetti correlation-energy formula into a functional of the electron density*. Physical Review B, 1988. **37**(2): p. 785-789.
28. Becke, A.D., *Density-functional thermochemistry. III. The role of exact exchange*. The Journal of Chemical Physics, 1993. **98**(7): p. 5648-5652.
29. Martin, R., *Electronic Structure: Basic Theory and Practical Methods*. 2004.
30. Mulliken, R.S., *Electronic Population Analysis on LCAO[Single Bond]MO Molecular Wave Functions. I*. The Journal of Chemical Physics, 1955. **23**(10): p. 1833-1840.
31. Zhang, R.Q., C.S. Lee, and S.T. Lee, *The electronic structures and properties of Alq₃ and NPB molecules in organic light emitting devices: Decompositions of density of states*. The Journal of Chemical Physics, 2000. **112**(19): p. 8614-8620.
32. Wyckoff, R.W.G., *Crystal Structures*. 2nd ed. Vol. 1. 1963, New York: Interscience Publishers. 85-237.
33. Schaller, R.D., et al., *High-Efficiency Carrier Multiplication and Ultrafast Charge Separation in Semiconductor Nanocrystals Studied via Time-Resolved Photoluminescence†*. The Journal of Physical Chemistry B, 2006. **110**(50): p. 25332-25338.
34. Valiev, M., et al., *NWChem: A comprehensive and scalable open-source solution for large scale molecular simulations*. Comp. Phys. Commun., 2010. **181**(9): p. 1477-1489.

35. Hay, P.J. and W.R. Wadt, *Ab initio effective core potentials for molecular calculations. Potentials for K to Au including the outermost core orbitals*. J. Chem. Phys., 1985. **82**(1): p. 299-310.
36. Hariharan, P.C. and J.A. Pople, *The influence of polarization functions on molecular orbital hydrogenation energies*. Theor. Chem. Accounts Theor. Comput. Model (Theor. Chim. Acta), 1973. **28**(3): p. 213-222.
37. Francl, M.M., et al., *Self-consistent molecular orbital methods. XXIII. A polarization-type basis set for second-row elements*. J. Chem. Phys., 1982. **77**(7): p. 3654-3665.
38. Albert, V.V., et al., *Electronic Structure of Ligated CdSe Clusters: Dependence on DFT Methodology*. J. Phys Chem. C, 2011. **115**(32): p. 15793-15800.
39. Perdew, J.P., K. Burke, and M. Ernzerhof, *Generalized Gradient Approximation Made Simple*. Phys. Rev. Lett., 1996. **77**(18): p. 3865-3868.
40. Perdew, J.P., K. Burke, and M. Ernzerhof, *Generalized Gradient Approximation Made Simple [Phys. Rev. Lett. 77, 3865 (1996)]*. Phys. Rev. Lett., 1997. **78**(7): p. 1396-1396.
41. Becke, A.D., *Density-functional thermochemistry. III. The role of exact exchange*. J. Chem. Phys., 1993. **98**(7): p. 5648-5652.
42. Yang, P., et al., *Quantum chemistry of the minimal CdSe clusters*. J. Chem. Phys., 2008. **129**(7): p. 074709-12.
43. VMD. Available from: <http://www.ks.uiuc.edu/>.
44. Jose, R., et al., *Structure–Property Correlation of CdSe Clusters Using Experimental Results and First-Principles DFT Calculations*. J. Amer. Chem. Soc., 2005. **128**(2): p. 629-636.
45. Kasuya, A., et al., *Ultra-stable nanoparticles of CdSe revealed from mass spectrometry*. Nat. Mater., 2004. **3**(2): p. 99-102.
46. Nguyen, K.A., P.N. Day, and R. Pachter, *Understanding Structural and Optical Properties of Nanoscale CdSe Magic-Size Quantum Dots: Insight from Computational Prediction*. J. Phys. Chem. C, 2010. **114**(39): p. 16197-16209.

47. Kudera, S., et al., *Sequential Growth of Magic-Size CdSe Nanocrystals*. J. Adv. Mater., 2007. **19**(4): p. 548-552.
48. Yu, M., et al., *First principles study of CdSe quantum dots: Stability, surface saturations, and experimental validation*. Appl. Phys. Lett., 2006. **88**(23): p. 231910-3.
49. Troparevsky, M.C., L. Kronik, and J.R. Chelikowsky, *Ab initio absorption spectra of CdSe clusters*. Phys. Rev. B, 2001. **65**(3): p. 033311-033314.

Appendix

A1. Geometry Optimization of Bare and Passivated QDs

Four sizes of Cd_nSe_n Quantum Dots (QD) have been considered for our investigation, with 'n' = 6, 12, 13, and 33. They were cut directly from the CdSe würtzite bulk crystal³², and then relaxed using a conjugate gradient algorithm to the lowest total energy configuration. The coordinates of the optimized structure are documented in the independent file named as coordinates.txt. All of our calculations were performed on NWCHEM 6.0 program³⁴. The basis sets, LANL2DZ³⁵ and 6-31G*^{36, 37}, have been employed for CdSe and ligands, respectively. This choice of basis sets has proved to be a pragmatic but sufficient balance between accuracy and computational intensity³⁸. Both PBE^{39, 40} and B3LYP⁴¹ exchange and correlation (XC) functionals have been applied for DFT geometry optimization. In order to reduce the energy state degeneracy, the symmetry is suppressed during the simulation. Since the geometry optimization could only reach a local minimum, we control the error by repeating the relaxation from different starting coordinates of surfactants. In Table A. 1 and Table A. 2, we present the bond length, HOMO-LUMO gap and binding energy of bare and passivated QDs. Two XC functionals, PBE and B3LYP, show the same trend for all of the species tested. The B3LYP functional results in a slightly smaller HOMO-LUMO gap and binding energy of ligand than does the PBE functional, and also obtains a quantitatively better description for the bond length and a closer fit to reference results than the analogous use of the PBE functional.

A2. Optical Properties of Bare and Passivated QDs

According to the conclusion from reference¹⁴ the many-body correlations significantly change the spectra of ligands. Thus, a TDDFT calculation has been carried out in order to compute the optical spectra of ligated QDs. Table A. 3 demonstrates the decomposition of the main TDDFT excited-states of Cd_6Se_6 with four ligands. As we can see, most of the orbitals involved are localized on the Cd_6Se_6 QDs. This fact accounts for the minor dependence of the gap in ligand length. The passivation shifts the optical spectra of bare Cd_6Se_6 to the blue by ~ 0.2 eV.

Table A. 1: Band gap value and binding energy per Cd-Se pair for different sized bare CdSe quantum dots. All the quantum dots have been relaxed using PBE and B3LYP functional, respectively. The B3LYP functional results in a slightly smaller HOMO-LUMO gap and binding energy per CdSe pair than does the PBE functional. The band gap values for Cd₆Se₆ and Cd₁₃Se₁₃ obtained by using the B3LYP functional are 3.14 eV and 3.06 eV, respectively, which are in good agreement with earlier results^{17, 18, 44}.

		Cd ₆ Se ₆	Cd ₁₂ Se ₁₂	Cd ₁₃ Se ₁₃	Cd ₃₃ Se ₃₃
HOMO-LUMO	PBE ³	3.22	2.08	3.11	2.58
Gap (eV)	B3LYP	3.14	2.10	3.06	2.52
Binding Energy per	PBE	3.728	3.649	3.938	4.114
CdSe pair (eV)	B3LYP	3.175	3.107	3.398	3.558

³ The gap value is calculated with the B3LYP functional on the structure relaxed by PBE functional.

Table A. 2. Cd_nSe_n ($n = 6, 12, 13, 33$) + Ligands calculated by using the PBE and B3LYP functional theories with the LANL2DZ/6-31G* (CdSe/Ligand) basis sets. Two XC functionals, PBE and B3LYP, show the same trend in all of the QDs tested. The B3LYP functional results slightly in a smaller HOMO-LUMO gap and binding energy of ligand than the PBE functional does. The average bond length of Cd_6Se_6 has been computed to be 2.699 Å / 2.862 Å for intra/inter layer Cd-Se by using the B3LYP functional, which are consistent with the results of P. Yang¹⁷ and A. Kuznetsov¹⁸. Use of the B3LYP functional results in a quantitatively better description for the bond length and a closer fit to reference results than analogous use of the PBE functional. Thus, all of our later discussion is based on the geometry relaxed by using the B3LYP functional.

System	Ligands	DFT XC Functional	Bond Length (Å)		BE of Cd-L (kcal/mol)	H-L Gap (eV)
			Cd-Se (intra/intra(L)/inter/inter(L))	Cd-L		
Cd_6Se_6^4	Bare	PBE	2.709/ -- /2.861/ --	--	--	3.22
		B3LYP	2.699/ -- /2.862/ --	--	--	3.14
	Cys	PBE	2.703/2.727/2.826/2.947	2.859	-13.318	3.47
		B3LYP	2.693/2.717/2.828/2.950	2.876	-10.612	3.39
	MPA	PBE	2.705/2.730/2.821/2.930	2.847	-13.337	3.49
		B3LYP	2.696/2.720/2.820/2.926	2.846	-11.538	3.41

⁴ The Cd-Se bond length of ligated Cd_6Se_6 is classified as “intra/intra(L)/inter/inter(L)”, representing for intra layer bond, intra layer bond adjacent to the ligand, inter layer bond and inter layer bond adjacent to ligand, respectively.

System	Ligands	DFT XC Functional	Bond Length (Å)		BE of Cd-L (kcal/mol)	H-L Gap (eV)
			Cd-Se (intra/intra(L)/inter/inter(L))			
Cd₆Se₆	HSCH(NH ₂)	PBE	2.703/2.745/2.820/2.911		2.772	3.54
	-COOH	B3LYP	2.693/2.733/2.821/2.913		2.795	3.45
	HSCH ₂ COOH	PBE	2.708/2.731/2.807/2.938		2.844	3.48
		B3LYP	2.698/2.723/2.807/2.936		2.858	3.41
Cd₁₂Se₁₂	Bare	PBE	2.951/2.712/2.814/2.539		--	2.08
		B3LYP	2.972/2.703/2.806/2.535		--	2.10
	Cys	PBE	2.899/2.712/2.782/2.567		2.847	2.35
		B3LYP	2.929/2.705/2.768/2.558		2.855	2.38
	MPA	PBE	2.906/2.716/2.778/2.561		2.828	2.37
		B3LYP	2.930/2.708/2.765/2.556		2.837	2.39
Cd₁₃Se₁₃	Bare	PBE	2.785/2.702/3.016/2.806		--	3.11
		B3LYP	2.778/2.693/3.102/2.801		--	3.06
	Cys	PBE	2.777/2.728/2.912/2.821		2.855	3.35
		B3LYP	2.764/2.705/3.050/2.822		2.908	3.27

System	Ligands	DFT XC Functional	Bond Length (Å)		BE of Cd-L (kcal/mol)	H-L Gap (eV)	
			Cd-Se (intra/intra(L)/inter/inter(L))				Cd-L
Cd ₁₃ Se ₁₃	MPA	PBE	2.783/2.717/2.902/2.846		2.858	-14.447	3.31
		B3LYP	2.773/2.699/3.034/2.843		2.885	-11.763	3.26
	HSCH(NH ₂)-COOH	PBE	2.767/2.728/2.921/2.845		2.795	-17.920	3.37
		B3LYP	2.755/2.702/3.046/2.845		2.856	-14.446	3.28
	HSCH ₂ COOH	PBE	2.784/2.724/2.906/2.838		2.850	-14.470	3.34
		B3LYP	2.765/2.700/3.046/2.840		2.885	-11.999	3.25
Cd ₃₃ Se ₃₃	Bare	PBE	2.868/2.738/2.739/2.760		--	--	2.58
		B3LYP	2.869/2.732/2.730/2.756		--	--	2.52
	Cys	PBE	2.814/2.799/2.938/2.766		2.862	-17.382	2.84
		B3LYP	2.804/2.763/2.955/2.802		2.874	-12.179	2.80
	MPA	PBE	2.807/2.762/2.940/2.839		2.878	-13.262	2.85
		B3LYP	2.800/2.758/2.949/2.814		2.895	-9.039	2.79

Table A. 3: Decomposition of the representative TDDFT excited-states of Cd_6Se_6 with four ligands. Most of the orbitals possessing dominant contributions to the excitations are localized on the Cd_6Se_6 QDs rather than on the ligands. This observation agrees well with Kilina's work ¹⁴. This observation could therefore explain the relatively minor influence of different ligands upon the observed absorption spectrum. For bare and capped Cd_6Se_6 , all of the transitions occurred among the same orbitals (Here the degenerate states are considered as the same states). Hence, the surface passivation shifts the optical spectra of the bare Cd_6Se_6 QDs to the blue by ~ 0.2 eV.

System	Energy (eV)	Oscillator Strength	Excited-State Composition	
			Percentage of Contribution	Involved Orbitals
Bare Cd_6Se_6	2.66	0.0684	97%	H-2 (Se 4p) — L (Cd 5s, Se 5s)
	3.15	0.0768	61%	H-7 (Se 4p) — L
			23%	H (Se 4p) — L+1 (Cd 5s)
			61%	H-8 (Se 4p) — L
	3.15	0.0765	23%	H-1 (Se 4p) — L+1
			34%	H — L+1
			33%	H-1 — L+1
	3.32	0.0456	34%	H-1 — L+1

System	Energy (eV)	Oscillator Strength	Excited-State Composition	
			Percentage of Contribution	Involved Orbitals
Bare Cd ₆ Se ₆			33%	H — L+1
	3.82	0.0355	42%	H — L+3 (Cd 5s, Se 4p, 5s)
			34%	H-3 (Se 4p) — L+2
	4.12	0.0254	50%	H-4 — L+2
			20%	H-3 — L+3
Cys	2.84	0.0635	84%	H-2 — L (Cd 5s, Se4p)
	3.37	0.1294	55%	H-7 (Se 4p) — L
	3.37	0.1241	55%	H-8 (Se 4p) — L
	3.94	0.0372	33%	H-10 (N 2p) — L
			24%	H-1 (Se 4p) — L+3 (Cd 5s, 4p, Se 4p, 5s)
			17%	H (Se 4p) — L+2 (Cd 5s, 4p, Se 4p, 5s)
	4.09	0.0258	36%	H-3 (Se 4p) — L+1 (Cd 5s)

System	Energy (eV)	Oscillator Strength	Excited-State Composition	
			Percentage of Contribution	Involved Orbitals
Cys	4.09	0.0248	37%	H-4 (Se 4p) — L+1
	4.24	0.0216	26%	H-5 (Se 4p) — L+2
			21%	H-6 (Se 4p) — L+3
	4.30	0.0384	25%	H-2 (Se 4p) — L+6 (Cd 4p, Se 4p, 5s)
MPA	2.86	0.0673	96%	H-2 (Se 4p) — L (Cd 5s, Se 5s)
	3.38	0.1362	85%	H-5 (Se 4p) — L
	3.38	0.1362	85%	H-6 (Se 4p) — L
	3.99	0.0522	29%	H-10 (Se 4p) — L
			21%	H-1 (Se 4p) — L+2 (Cd 5s, 4p, Se 5s, 4p)
			21%	H (Se 4p) — L+3 (Cd 5s, 4p, Se 5s, 4p)
	4.15	0.0214	41%	H-4 (Se 4p) — L+2
			41%	H-3 (Se 4p) — L+2

System	Energy (eV)	Oscillator Strength	Excited-State Composition	
			Percentage of Contribution	Involved Orbitals
SHCH(NH ₂)COOH	2.89	0.0682	96%	H (Se 4p) — L (Cd 5s, Se 5s)
	3.37	0.0273	64%	H-8 (Se 4p) — L
			18%	H-6 (Se 4p) — L
	3.37	0.0274	64%	H-9 (Se 4p) — L
			18%	H-5 (Se 4p) — L
	3.40	0.1059	69%	H-5 — L
			23%	H-9 — L
	3.40	0.1059	69%	H-6 — L
			23%	H-8 — L
	4.08	0.0564	43%	H — L+6 (Cd 5s, S 3p, C 2s)
4.15	0.0217	18%	H-4 (Se 4p) — L+2 (S 3s 3p, C 2s, 2p)	
		18%	H-3 (Se 4p) — L+3 (S 3s 3p, C 2s, 2p)	

System	Energy (eV)	Oscillator Strength	Excited-State Composition	
			Percentage of Contribution	Involved Orbitals
SHCH(NH₂)COOH	4.21	0.0205	41%	H-5 — L+1 (Cd 5s, S 3s 3p, C 2s, 2p)
	4.21	0.0205	41%	H-6 — L+1
SHCH₂COOH	2.85	0.0649	96%	H-2 (Se 4p) — L (Cd 5s, Se 5s)
	3.38	0.1219	47%	H-6 (Se 4p) — L
			40%	H-7 (Se 4p) — L
			47%	H-5 (Se 4p) — L
	3.38	0.1219	40%	H-8 (Se 4p) — L
			29%	H-10 (Se 4p) — L
			19%	H-1 (Se 4p) — L+2 (Cd 5s, 4p, Se 5s, 4p)
	3.98	0.047	19%	H (Se 4p) — L+3 (Cd 5s, 4p, Se 5s, 4p)
			41%	H-4 (Se 4p) — L+2
41%			H-3 (Se 4p) — L+3	

System	Energy (eV)	Oscillator Strength	Excited-State Composition	
			Percentage of Contribution	Involved Orbitals
SHCH ₂ COOH	4.15	0.0366	26%	H-3 — L+1 (Cd 5s, Se 5s, 4p)
			25%	H-4 — L+3
			24%	H-3 — L+2
	4.15	0.0366	26%	H-4 — L+1
			24%	H-4 — L+2
			24%	H-3 — L+3
	4.34	0.0254	31%	H-6 (Se 4p) — L+1
			18%	H-2 — L+4 (Cd 5s, 4p, Se 5s, 4p)
	4.34	0.0254	31%	H-5 (Se 4p) — L+1
			18%	H-2 — L+5 (Cd 5s, 4p, Se 5s, 4p)
4.44	0.0259	59%	H-12 (Se 4p) — L	